ABSTRACT

DENEKE, JOSEPH ALEXANDER. Multirotor Wake and Turbulence in the Presence of Crossflow Gust. (Under the direction of Dr. Darius Carter).

With rotorcraft forms of Urban Air Mobility (UAM) becoming increasingly popular, the need to understand rotorcraft wake dynamics and turbulence for reasons pertaining to safety is becoming very important within today's modern aerospace industry. It is important to be able to characterize and estimate the effects rotor wake, and more specifically, rotor tip vortices on an air vehicle that could be flying within close proximity to the vehicle in question. Furthermore, a gap in the knowledge of rotor wake dynamics exists when analyzing rotor wake in the presence of flow with a crosswind component. The flow interactions of these two aerodynamic phenomena are not completely understood yet, and research in this area is necessary to implement wide-scale use of UAM in today's busy world.

The low-level understanding of these interactions is greatly related to the concepts of turbulence statistics and vortex dynamics. This project aims to understand these interactions better by using a highly precise experimental aerodynamics and a 7- approach hole 3-D velocity probe sensor. To simulate a forward flight situation for a rotorcraft air vehicle, the North Carolina State University (NCSU) subsonic wind tunnel is utilized. To simulate a crossflow gust impingement on the rotorcraft air vehicle wake, a crossflow gust generator, developed by NCSU undergraduate researchers, was developed and implemented in the experiments.

Quantification of the turbulence intensity dissipation showed that crossflow has a positive effect on wake turbulence dissipation; that is, when a crossflow impinges on a wake, the trailing tip vortex strength dissipates faster than in the normal forward flight case without crossflow. Experimental results also showed that a given tip vortex core displaces with a certain velocity and acceleration profile when subjected to a crossflow gust impingement.

Multirotor Wake and Turbulence in the Presence of Crossflow Gust

by
Joseph Alexander Deneke

A thesis submitted to the Graduate Faculty of
North Carolina State University
in partial fulfillment of the
requirements for the degree of
Master of Science

Aerospace Engineering

Raleigh, North Carolina
2024

APPROVED BY:

_____	_____
Dr. Jack Edwards	Dr. Ashok Gopalarathnam

_____
Dr. Darius Carter
Chair of Advisory Committee

DEDICATION

To my parents, grandparents, family, and friends for all their support. To Dr. Darius Carter for his endless support, dedication, and time.

BIOGRAPHY

The author was born in Virginia Beach, Virginia, where he spent most of his life growing up, with a three-year move to Naples, Italy. Joseph has always had a love for airplanes, fighter jets, and anything aviation-related since he was just five years old. In May of 2022, Joseph graduated with a Bachelor of Science in Mechanical Engineering with a concentration in Aerospace Engineering from George Mason University. He then went on to pursue a Master of Science in Aerospace Engineering at NCSU under the advising of Dr. Daius Carter. Upon completion of his degree, he will continue his education by pursuing a Ph.D. in Aerospace Engineering through the SMART scholarship program at NCSU, in conjunction with Naval Air Warfare Center (NAVAIR). Throughout most of Joseph's higher education, he worked during the summers as a Mechanical and Aerospace Engineering intern for Naval Sea Warfare Center (NSWC), Dahlgren, VA, and NAVAIR, Patuxent River, respectively.

ACKNOWLEDGMENTS

I would like to thank my advisor Dr. Darius Carter for providing me with the great opportunity to work as his first graduate student as an assistant professor, and for all his time, support, and guidance throughout this challenging research project. During this project, he was always available to provide assistance and help whenever needed. His knowledge of experimental fluid mechanics and rotor wing aerodynamics has greatly contributed to the knowledge used in this project, and I am forever grateful for this. I would like to thank my committee members Dr. Jack Edwards and Dr. Ashok Gopalarathnam for their expert knowledge in aerodynamics and fluid mechanics. Throughout the combined five graduate courses I have taken with them, I successfully gained an immense understanding of the disciplines of aerodynamics, fluid mechanics, and turbulence which have allowed me to succeed in this project.

I would also like to thank my family, friends, and DoD supervisors for supporting me through graduate school and pursuit of a Master's Degree. Finally, I would like to thank the five undergraduate research assistants, Jimmy-Lee Brown, Ben Ashley, John Gillespie, Zach Kocan, and Noah Prevatte, who have helped me tremendously with my project, from experimental setup to experimental post-processing.

TABLE OF CONTENTS

LIST OF TABLES

LIST OF FIGURES

NOMENCLATURE

V_∞	Forward flight/edgewise/wind tunnel velocity
V_{tip}	Rotor tip velocity
U_{cross}	Crossflow velocity
x, y, z	Longitudinal, lateral, vertical direction
S	Rotor separation distance
u, v, w	Longitudinal, lateral, vertical velocity
u'	Velocity fluctuation
$\left\|\vec{V}\right\|$	Velocity magnitude (speed)
I	Turbulence intensity
ΔI_{P1-P4}	Turbulence intensity decay value
u_{rms}	Root-mean-squared velocity
Re_{tip}	Rotor tip Reynolds number
ν	Kinematic viscosity
V_θ	Vortex tangential velocity
Γ	Vortex strength
ω	Angular velocity
M_{tip}	Rotor tip Mach number
a	Speed of sound
R_r, R	Rotor radius
μ	Advance ratio
α_{plr}	Rotor tilt angle (relative to horizontal)
N_b	Number of Blades
c_r	Root chord
σ	Solidity
λ	Raper ratio
θ_0	Pitch angle
$\Delta\theta_{tw}$	Twist angle
Ψ	Azimuth angle
τ_u	Integral time scale
CF	Crossflow
P1	Plane 1, etc.
$u'u'$	Variance
$u'v'$	Covariance

CHAPTER 1. Introduction

Urban Air Mobility

In recent years, the aerospace industry has pushed for the development of new methods of Urban Air Mobility (UAM) that will change the industry forever. There is a need to transport people from urban districts to airports in suburban areas more efficiently through the use of electric vertical takeoff & landing (EVTOL) aircraft. Companies such as Lilium, Wisk, and Archer are in the flight test phases for new designs of EVTOL aircraft that will be implemented in the commercial market in the coming decades. These types of aircraft and new modes of transportation will be the new 'Uber' or 'Lift' for people trying to get from one place to another. Not only will UAM-based aircraft make public transportation easier for the general public, but it will also make airline transportation more accessible. A study in the past decade showed that, in the United States, the average distance a person must travel to get to the closest commercial airport is nearly 26 miles [1]. For the average person, this distance is not feasible from both the perspectives of time and the cost of transportation. EVTOLs and other UAM methods could open up the accessibility for these people to get to the airport more easily.

Motivation

With this increased demand for the implementation of various types of EVTOLs, there are induced adverse effects. Airspace in urban areas will become increasingly cluttered as EVTOLs begin to take the place of taxis, Ubers, etc. With the current state of ground-based transportation, aerodynamic effects of one car on another are a non-factor. If anything, driving in the wake of a larger car can decrease the fuel consumption of the vehicle in the wake [2]. In the current state of UAM and EVTOL technology, most vehicles are propelled by propellors or rotors in a high-advance-ratio edgewise flight regime. With this, safety concerns relating to wake turbulence and downwash interactions become more prominent, as shown in Nguyen et al. [3]. Air vehicles flying into the turbulent downwash of rotor wing vehicles can cause instabilities and can sometimes lead to crashes or other pedestrian-related mishaps [4] [5].

In certain cases, wake turbulence can lead to catastrophic events. In November 2001, an American Airlines Airbus 300 with flight number AA 587 took off from JFK, encountered severe wake turbulence, and crashed as a result of poor corrections from pilot error, killing hundreds of people. In the investigation, it was found that severe wake turbulence was encountered from a Boeing 747 that had taken off just prior to AA 587. Interestingly, the 747's flight path was much

further north of AA 587, but it was found that a strong crosswind was present at the time of these flights. As shown in the figure below, the 747's (JAL47) wake was subjected to a nearly perpendicular crosswind of 11 knots, which moved the wake into the flight path of AA 587 [6].

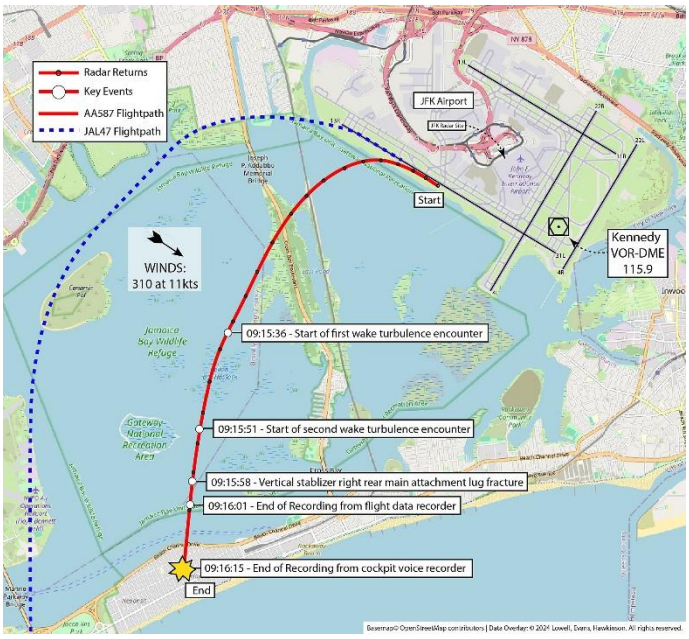

Figure 1.1. AA 587 flight path and crash map recreation [7].

Prior to this accident, if there had been an overall better understanding of the movement of wake turbulence with crosswind, this situation could have been easily avoided with a warning alert given to air traffic controllers before the takeoff of AA 587.

With more cluttered airspace becoming a normality in the coming years, it will be essential for the aerospace industry to understand these wake turbulence interactions at the lowest levels and to build in safety mechanisms to prevent incidents like this from happening.

Open Questions

Many studies have been completed on general rotor-wing wake turbulence aerodynamics (large-scale turbulence), and these interactions are well understood. While comprehensive studies of rotor wing tip vortex aerodynamics have been completed, there is currently a gap in the understanding of how vortices behave under the influence of a crossflow gust or a crosswind. In general, there are little to no studies on how vortices travel under the influence of wind. This specific scenario will prove to be important for the greater understanding of the aerodynamics of densely populated UAM airspaces of the future.

While displacement and position of vortices upon the influence of wind is important to understand, it is also important to understand how the strength of a given vortex filament changes under the influence of wind. In summary, the questions to be answered in this project are as listed below:

In the presence of a constant velocity perpendicular crossflow gust:

1.) How do rotor wing tip vortices probate downstream?
    a. How do the lateral (y) and longitudinal (x) positions of these vortices change?
2.) How does the strength of the tip vortices change downstream of the rotors?
    a. Quantify the results of changing vortex strength/turbulence intensity in the far field.
    b. How does the vortical induced velocity (also tangential velocity, v_θ) change with increasing longitudinal (x) distance from the rotor?
3.) How does the rotor downwash distribution lateral position change downstream?
    a. Given a forward flight and crossflow gust speed, how safe would it be to operate another air vehicle at various distances behind the vehicle in question?

Experimental Goals

The study presented in this project aims to perform a comprehensive understanding of vortex propagation downstream of rotors in edgewise forward flight using various experimental fluid dynamics techniques. We are particularly interested in how the physical location of tip vortices changes under the transient influence of a constant crossflow gust, as well as how the vortex strength changes over time with this gust applied. This project will provide us with a valuable understanding of multirotor vortex effects, all for the greater goal of increased safety in the congested airspaces of the future.

Experimental Hypothesis

The following three experimental hypotheses have been made:

1.) When the wake of a rotor is subjected to an oblique flow velocity component of V_∞ and a uniform crossflow velocity of U_{cross} is applied perpendicularly directly behind the rotor disk, any given trailing vortex core will propagate with a 2-D velocity of $\vec{V}_{core} = V_\infty \hat{\imath} - U_{cross}\hat{\jmath}$. For determining the position of said given trailing vortex laterally (y) and longitudinally (x), one can multiply the velocity $\left|\vec{V}_{core}\right|$ by the time, t that the crossflow

has acted on the trailing vortex. The following equations and figure show this kinematics problem in a visual form.

$$\vec{V}_{core} = \vec{V}_{wind} = [V_\infty]\hat{\imath} - [U_{cross}]\hat{\jmath} \quad (1)$$

$$\Delta\vec{X}_{core} = \vec{V}_{core} \cdot t \quad (2)$$

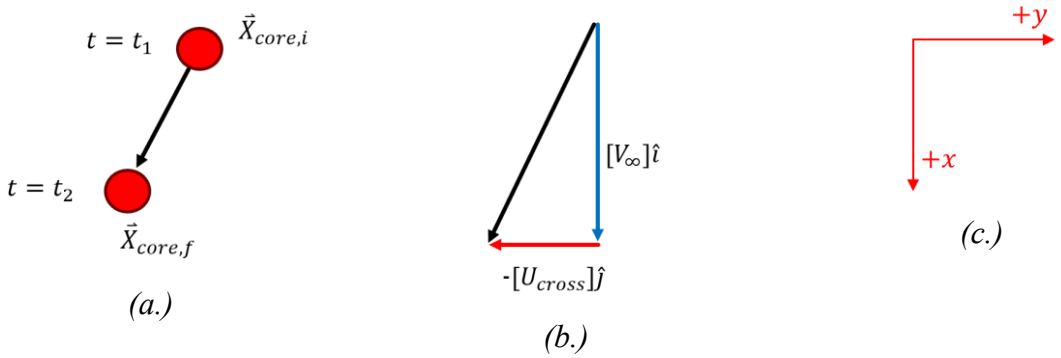

Figure 1.2. Vortex kinematics theory (a.) Vortex core displacement visualization. (b.) Edgewise/crossflow velocity triangle. (c.) Example coordinate system.

2.) The 3-D slipstream geometry will move with the same 2-D velocity of the trailing vortices, as the slipstream boundaries are defined by vortex cores.

3.) The downwash velocity distribution will propagate downstream with the same 2-D velocity.

4.) Tip vortices and large-scale wake turbulence will be stronger for a zero-taper, constant chord planform than a tapered planform rotor.

CHAPTER 2. Previous Work

Preface

The motivation behind past and current research on rotor tip vortex dynamics and wake modeling stems from a push to advance the current understanding of how futuristic UAM vehicles will affect each other when flying in close proximity near each other. Delving deeper, there is a gap of knowledge in completed previous work in the specific area of crosswind and crossflow interactions of rotor tip vortices. With this being said, there is a significant amount of previous research completed on rotor tip vortex propagation downstream of a rotor in hover and in forward flight. These efforts have produced analytical solutions for slipstream geometry, downwash distributions, and tangential velocity distributions or a rotor in hover and forward flight. This work and associated literature have established a solid foundation for the work completed in this thesis, some of which is discussed briefly in this chapter.

UAM Wake Analysis

As discussed in the previous chapter, a major push has been made in the aerospace industry to begin using EVTOL aircraft to transport people from place to place. As EVTOLs gain in popularity and EVTOL traffic becomes noticeable, the wake interactions between vehicles will be important to analyze for safety reasons. Preliminary analysis has been completed on this topic in [3]. On a rotor wing aircraft, strong tip vortices form in a very similar fashion to that of a fixed-wing aircraft; high suction pressure on the upper surface of a wing meets the high positive pressure on the lower surface at the tip, causing a "rolling-up" of the flow to occur [8]. While tip vortex interactions are the primary focus of this thesis, smaller vortex shedding occurs at inner radial points, which turns into 'vortex sheets'. It is important to note that these are areas of elevated turbulence kinetic energy and can affect the flight dynamics of nearby air vehicles [9] [10]. At a high level, it has been found that wake turbulence can produce unexpected rolling moments to nearby-flying air vehicles if the proper time is not allotted for the turbulence to dissipate. For this reason, crashes such as [11] have occurred.

Rotor Wake Dynamics

At a high level, the fluid dynamics of the wake for rotor-propelled air vehicles has been well understood for many decades. Cases of hover and forward (also referred to as oblique flow) flight have been studied on numerous occasions in great depth. Advances in computational efficiency have been made in more recent decades that have allowed the industry to gain a much more holistic

visualization of rotor tip vortices, and their dynamics below the rotor for the case of hover, or in the Trefftz plane for the case of forward flight. Some of this work is outlined in ref [12] [13] [14]. From these works, comparisons of vortex lattice method (VLM) codes to experimental results of tip vortex locations in the downstream of a rotor in hover were made, and they matched up nearly perfectly over a wide range of wake ages. It was also found that, due to viscous effects in the flow, it is difficult to measure wake characteristics and obtain accurate vortex data for flows that are over 7200 degrees of wake age. That is, generally, after 20 rotations of a rotor being analyzed, the vortices that were created at low wake ages less than 360 degrees will give invalid experimental results, as the viscous effects will have dissipated the vortices into large-scale turbulence.

Rotor Tip Vortex Dynamics

Numerous low-level, high-fidelity studies have been completed in recent decades that have allowed the industry to gain a very concrete understanding of how tip vortices propagate and evolve underneath a rotor disk plane in hover and forward flight. For the case of hover, characteristics of rotor tip vortex dynamics are well known.

Work completed by Martin et. al in [15] produced great results pertaining to the general geometry of the slipstream underneath a rotor in hover for moderately low Reynolds number cases, as well as much more specific features of tip vortices. This study was completed using a similar, but higher fidelity technique to PIV called laser doppler velocimetry (LDV). A rectangular, untwisted, single-blade rotor was examined under incompressible conditions to obtain vortex characteristics over increasing wake ages. Experimental results such as vortex tangential induced velocity were compared to analytical models such as the Lamb-Ossen wake model in this study. This model quantifies the vortex-induced tangential velocity v_θ of a rotor, given Γ_0 , R_r vortex core radius r_c the kinematic viscosity ν the time since the vortex spawn t and a model constant $\alpha_L = 1.25643$. This is shown in equation 3, below.

$$v_\theta = \Gamma_0 2\pi R_r \left[1 - e^{-\alpha_L \left(\frac{r}{r_c}\right)^2}\right]\left(1 - e^{-\frac{r^2}{4\nu t}}\right) \quad (3)$$

For experimental studies, it is common practice to resolve Γ and this analysis was completed in this study. A method used in literature for resolving Γ with a 7-hole velocity probe is presented in [16]. Depending on the sample rate of the 3-D velocity probe being used, this can allow the user to obtain a much more accurate quantification of turbulence measurements at a specific point in space over a given time than PIV would [17]. Similar methods will be employed

in this project, although, completely resolving Γ is a difficult task unless experimental grid domain density is incredibly small. Because of this, induced velocities from said Γ will be resolved more thoroughly. These aforementioned methods are very time-intensive and sometimes impractical. Using these experimental methods, Vortex-induced tangential velocity is an important parameter that should be measured over a wide range of wake ages to gain a better understanding of velocity distributions in the Trefftz Plane of a rotor, whether it is in hover or forward flight. Understanding of this parameter can provide insight into the severity of turbulence and freestream shears an air vehicle may experience when flying near a VTOL aircraft.

Work by Martin et al. produced several conclusions that are of significant relevance to this thesis. It was found that at this moderately Reynolds number of $272 \cdot 10^3$, the vortex core location moves inward radially by approximately 10% of the rotor radius length per 360 degrees of wage age. Within the first 3 degrees of wake age, there are two vortex roll-ups at the rotor tip, which then converge into one vortex for wake ages greater than 3 degrees. It was also found that vortex sheet spreading off the trailing edge of the rotor at inner radial locations is present significantly at wake ages that are less than 45 degrees. This is shown in the form of axial velocity deficit plots. As wake age reaches 360 degrees, vortex sheet turbulence is almost non-existent, and vortex-induced tangential velocities have dissipated by nearly 75% due to viscous effects.

Vertical locations of vortex rollups in the Trefftz plane are also of significant importance due to the effects they could have on vehicles flying in close vertical proximity to the rotor(s) in question. Work by Ansaripour et al. in [18] provides great insight into these rotor wake characteristics. In this work, a similar study to that of Martin et al. was completed, but with a highly twisted, moderately tapered rotor design.

A similar set of analytical solutions for slipstream geometry were compared to experimental results in this analysis, as shown in Langrebe and Bellinger's equations (4 - 6) below.

$$\frac{Z}{R_{Tip}} = k_1 \zeta_w \tag{4}$$

$$\frac{Z}{R_{Tip}} = \left(\frac{z_{tip}}{R}\right)_{\zeta_w = 2\pi/N_b} + k_2 \left(\zeta_w - \frac{2\pi}{N_b}\right) \tag{5}$$

Radial positions are found as follows:

$$\frac{X}{R_{Tip}} = A + (1 - A)\exp(-\Lambda \zeta_w) \tag{6}$$

Where:

$$k_1 = -0.25(C_T/\sigma + 0.001\Theta_{twist})$$

$$k_2 = -(1.41 + 0.0141\Theta_{twist})\sqrt{C_T/2}$$

By examining and comparing the slipstream and wake geometries at varying rotor rotational speeds, it was found that axial and vertical vortex roll-up locations have little to no dependence on the rotational speed of the rotor. For the prescribed Reynolds number and flight conditions, the vertical location of tip vortices was found to move downward with respect to the rotor plane by nearly 50% of the rotor radius through a wake age of 360 degrees.

Examination of the vortex cores by way of PIV and flow visualization also showed that there is a prominent region of laminar flow within a vortex. As wake age increases, this laminar region becomes progressively less noticeable, the vortex strength, Γ decreases, and a turbulent, deformed vortex survives.

The work presented thus far has only considered the scenario of a single rotor with any given number of blades. Work completed by Lee et al. in [19] provides insight into a similar study, but with 1-4 rotors in close proximity. In this study, some very important conclusions were drawn, of which many are relevant to this thesis. Downwash distributions and wake dynamics were found to be highly dependent on a non-dimensional rotor separation distance factor, denoted as $\frac{S}{R_r}$ in this study. For low to moderate Reynolds numbers, rotor-rotor interaction can almost be fully neglected for $\frac{S}{R_r} > 2$. It was also concluded that tip vortex interactions are much more prominent at $\frac{S}{R_r} < 2$, and the flow in these flight regimes is much more turbulent, chaotic, and unpredictable.

Oblique Flow Tip Vortex Dynamics

While it is important to understand the underlying characteristics of rotor tip vortex dynamics for a rotor in hover, there are many differences when analyzing a rotor in forward flight, or oblique flow. Firstly, and arguably most importantly, rotors in forward flight will always have some plane angle, α_{plr}. This angle represents the complementary angle of the rotor shaft to the freestream velocity plane, and it is required for this angle to be nonzero in order to create forward thrust. It is important to note that some literature denotes α_{plr} as the angle between the motor shaft and the freestream velocity, but this project will use the method aforementioned, opposite as in [20]. From this, the following equation can be used to describe the advance ratio of a rotor in forward flight, given a forward flight speed V_∞.

$$\mu = \frac{V_\infty cos(\alpha_{plr})}{\omega R_r} \tag{7}$$

Numerous computational and numerical studies have been completed relating to wake structures for rotors in forward flight, some of which are presented in [21] [22] and [23]. Many of the methods used in this literature are based on simple blade element momentum theory (BEMT) models or vortex lattice/panel methods, and the higher fidelity models are based on large eddy simulations (LES).

For general forward flight UAM dual-rotor configurations, it is highly favorable to configure the vehicle with counter-rotating blades for a few reasons. Firstly, the torques generated by two adjacent counter-rotating blades will cancel each other out. Also, due to the oblique flow velocity component, the flow velocity over any blade section will be a function of the azimuth angle [9]. Since most UAM vehicles do not use squash plates for cyclic control, this means there will be an uneven lift distribution for a configuration of two laterally adjacent rotors, causing a possible unwanted moment about the longitudinal axis of the air vehicle. Because of this reason, the rotors need to be configured in a way that the lifting moments about the longitudinal axis will cancel each other out [24].

Overall conclusions of these studies show that for lower order models (i.e. BEMT and vortex panel methods) used on rotors in forward flight, tip vortices act very similarly in the lateral and longitudinal directions as was discussed for hover. The major difference between hover and forward flight wake geometries lies in the vertical plane; due to the forward flight motion, tip vortices and vortex sheets stay relatively close to the rotor plane vertically compared to hover, where the tip vortices propagate downwards rapidly due to viscous effects. For LES-based simulations such as in [24], it was found that tip vortices decay and dissipate rapidly into generalized turbulence as compared to the hover scenario.

CHAPTER 3. Experimental Setup

Overview

The experimental setup for this project was designed and optimized to create the best possible combination of the following experimental parameters and design requirements:

1.) Rig shall fit within the test section of the NCSU subsonic wind tunnel.
2.) Rig shall be a dual rotor configuration with both rotors at the same longitudinal (x) location.
3.) Rig and wind tunnel combination shall allow optical access for PIV.
4.) Rig shall be designed for minimal wake disturbance.
    a. Little to no blunt edges on rotor rig.
    b. No holes or surface defects on walls between rotor rig and sensor planes.
5.) Rotor location shall be chosen so that the wind tunnel geometry has minimal effects on aerodynamic performance.
    a. Wind tunnel boundary layer impingement on rotors is nonexistent.
    b. Ground/ceiling/corner effects are negligible.
    c. Wind tunnel flow is fully developed at the longitudinal location of the rotors

With these experimental design conditions set early in the project, the rotor rig was designed to maximize the use of space within the wind tunnel while still meeting all design requirements. The figure below depicts the CAD render of the rotor rig placed inside the wind tunnel, as well as the actual rig placed inside the wind tunnel.

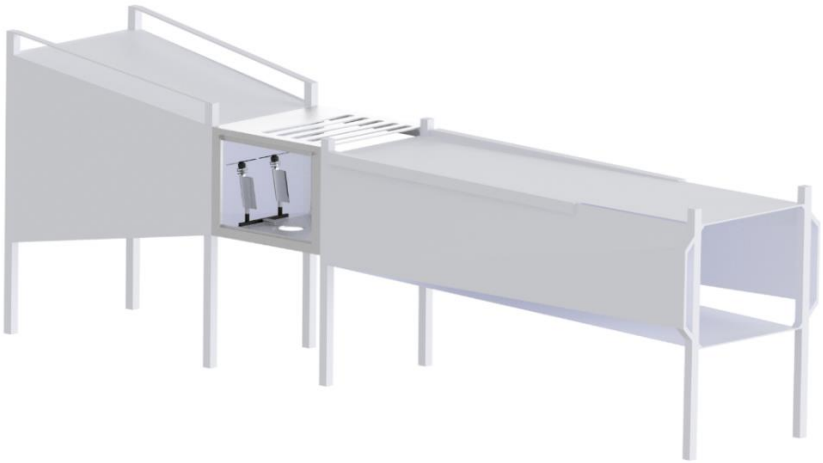

Figure 3.1. Wind tunnel CAD rendering of the experimental setup.

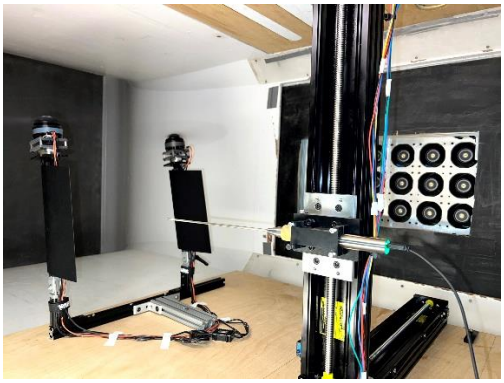

Figure 3.2. Experimental setup inside NCSU's subsonic wind tunnel.

The wind tunnel used in all experiments is a low-speed recirculating subsonic wind tunnel located in Engineering Building 3 at NCSU The dimensions of the utilized wind tunnel test section are 42"x45"x32". The maximum operating dynamic pressure is approximately 13.0 psf, and the temperature operating range is 65°F - 100°F. The documented turbulence intensity at the test section is 0.33%, but this value was calculated for these experiments, and the results are shown later in this thesis.

Rotor Selection

A major goal of the project is to analyze the difference in wake characteristics between varying rotor planforms. To achieve this goal, all experiments have been completed using two sets of rotor planforms. For all experiments, the same rotor planform has been implemented in a multirotor setup; in other words, rotor A was not analyzed in the same run as rotor B. A summary of key design features of both rotors is shown in table 3.1, below.

Table 3.1. Key rotor design features.

Parameter	Rotor A	Rotor B
N_b	2	2
R_r	13 in	13 in
c_r	1.125 in	0.9 in
σ	0.086	0.088
λ	0.56	1
θ_0	Varying	10°
$\Delta\theta_{tw}$	-10°	0°
Airfoil Shape	Commercial OTS	NACA 0020

Rotor A was purchased COTS, and the following figure depicts the rotor used in experiments.

Figure 3.3. Rotor A.

Rotor B was manufactured by way of 3-D printing with acrylonitrile butadiene styrene (ABS). The following figure depicts rotor B in multiple fashions.

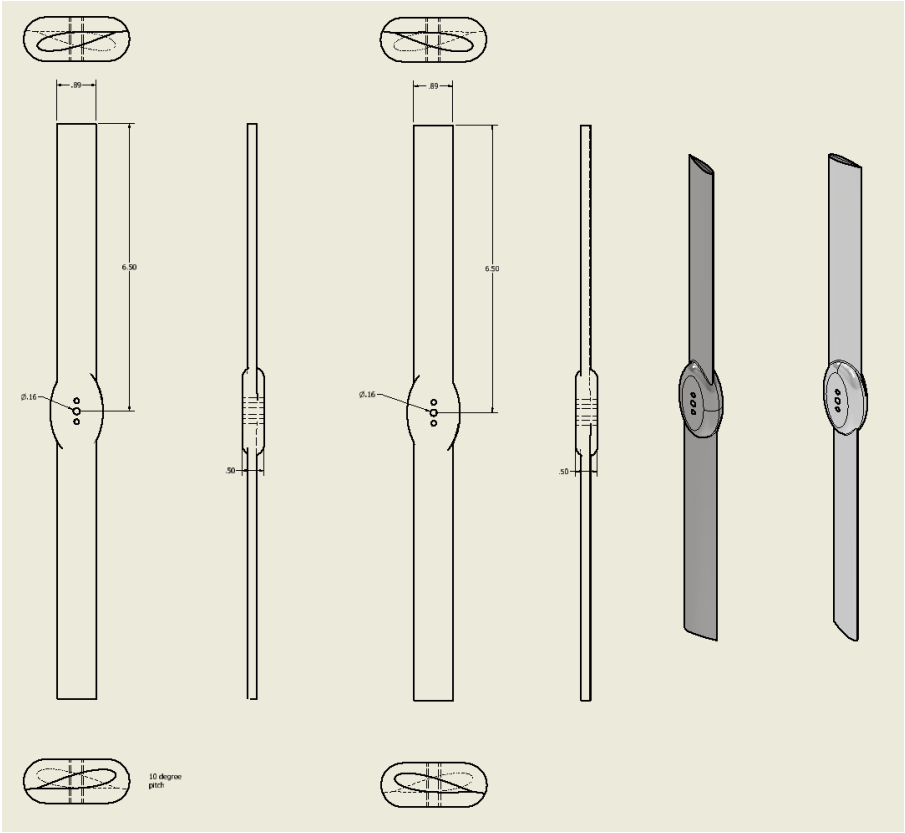

Figure 3.4. Rotor B drawing with dimensions (inches).

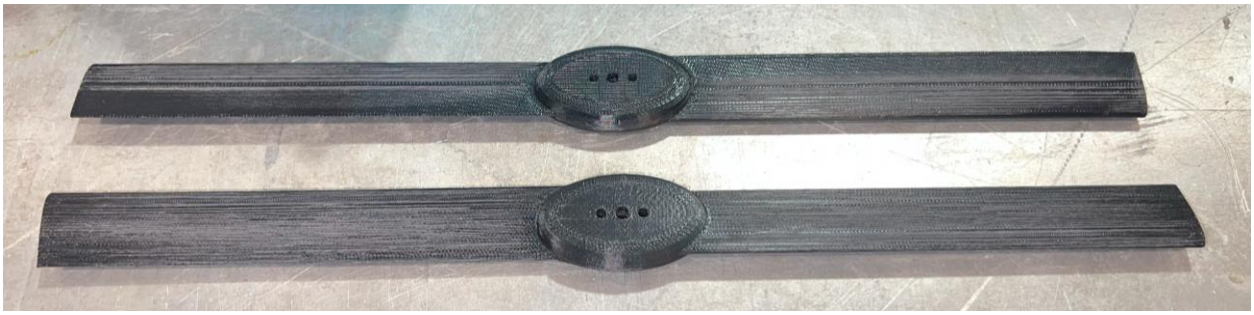

Figure 3.5. 3-D printed rotor B used in experiments.

For both rotors, a hub connection was chosen or designed to minimize the hub's wake signature. As shown in figures 3.4 and 3.5, both hubs have a minimal cross-sectional area, therefore it can be assumed that the wake produced by the hubs is present, but almost negligeable.

Rotor Rig

Much thought was put into the design of the rotor rig for these experiments. The most important aspect of the design of this component is its effect on the wake signature. In the most ideal scenario for a wake-analysis-based project, it is preferred to suspend the setup within the tunnel via a magnetic suspension system, similar to the method shown in Inomata, et al. [25]. Since this method is unavailable with the current resources, it is important to be conscious about the wake that will be coming off structures exposed to the freestream. Because of this, the rotor rig was designed as a dual-rotor test stand consisting of slotted t-brackets and two large wing fairings to smooth the flow over the brackets. The rotor rig is depicted in the CAD rendering shown in the figure below.

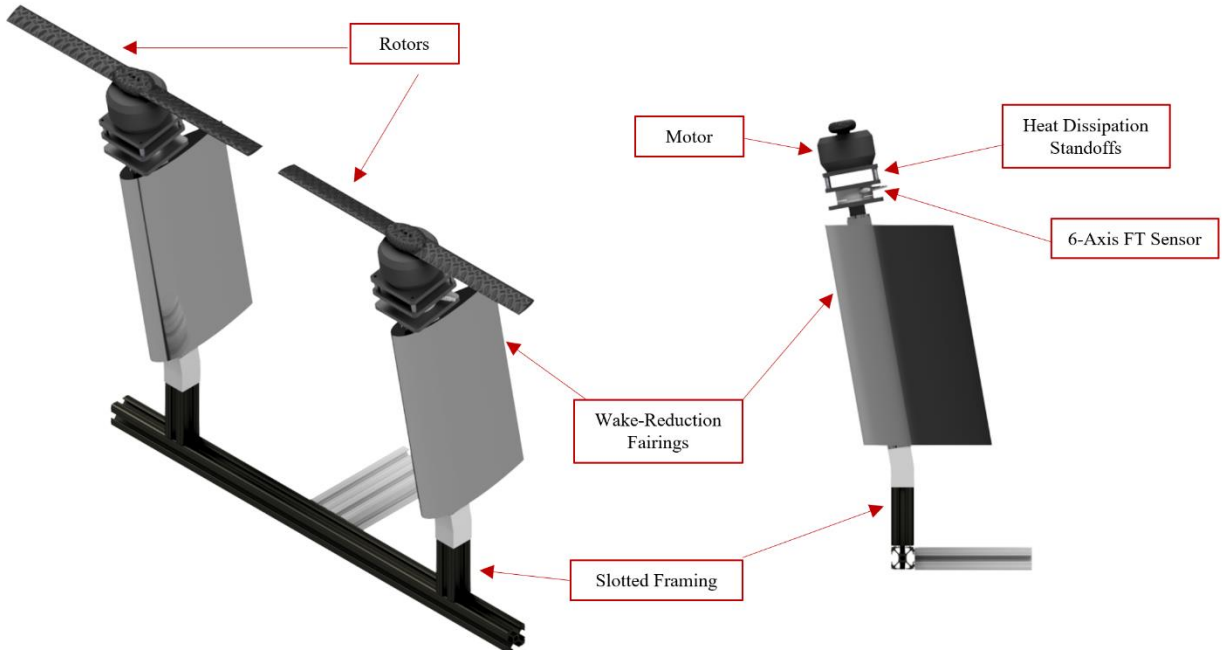

Figure 3.6. Rotor rig CAD rendering with component definitions.

As shown in figure 3.2, all electronics cables used in the experiments (motor power, hall effect connections, and FT/sensor cable) were passed through the wake-reduction fairing shown in figure 3.6 in an effort to reduce the trace of the cables on the wake. It will be shown below that the fairings were incredibly effective at reducing the effect on wake trace, and the only major wake

turbulence being produced from the rig originated from the motor connection plates and the base of the rig.

For all tests performed in this project, the rotors were introduced to an α_{plr} or forward tilt of 10°, which is a flight condition that is commonly found in the VTOL industry for forward flight. With this, the wake-reduction fairings were designed so that the airfoil section of the fairing wing is perfectly aligned with the flow; that is, there is zero incidence of the fairing with respect to the freestream wind in the tunnel. This primarily reduces the drag, and subsequently, Trefftz-Plane wake velocity distribution of the fairing, and it also allows the experimentalists to easily adjust the setup to exactly a 10° flight condition. The fairing was designed so that the maximum airfoil thickness is just 1% larger than the thickness of the frame. Finally, the fairing serves the dual purpose of also allowing ESC, hall effect sensor, and force-torque (FT) sensor cables to be unexposed to the freestream flow. All other components of the rotor rig such as connector plates were manufactured via 3-D printing and assembled into the final product shown in figure 3.2, above.

For both rotor configurations, it is important to note that the rotation directions between rotors are opposite each other. In the case of both rotor planforms, the advancing blade is on the geometric 'inside' inside of the wind tunnel, and the retreating blade is on the geometric 'outside' of the wind tunnel. Combining the effects of wind tunnel dimensional restrictions and previous research on rotor separation effects on aerodynamic performance, the rotor separation distance was set to a fixed value of 1.625 in. Dividing this value by the rotor radius yields a non-dimensional rotor separation distance of $S/R_r = 0.25$. It is important to note that all tests in this project are completed with the same rotor separation distance, and the effects of this separation distance are not examined or reported on in significant detail.

Crossflow Gust Generator

Throughout the course of this project, a parallel project was completed in the RARE lab. Undergraduate researchers Jimmy-Lee Brown and Ben Ashley designed and built a 2'x1' gust generator fan array that was used to simulate the crossflow gust in these experiments. The array consists of 18 fans configured in three rows and six columns. The array is powered by an external power supply, and is controlled via a pulse with modulation (PWM) output from two Arduino Unos. The generator runs on a 48V DC power supply, and has a maximum current output of 15.6 A. For the purposes of this project, the gust generator was run at a PWM of 0.5 Hz, which is the

lowest setting allowable by the manufacturer of the fans. With this being a new, untested piece of equipment, measurements of flow velocity and turbulence intensity were taken and are presented later in this document. Figure 3.7 depicts the 2'x1' gust generator used in this project.

(a.)

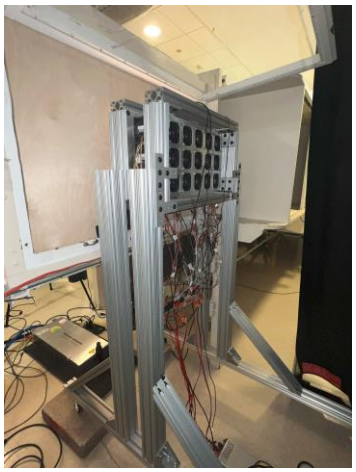

(b.)

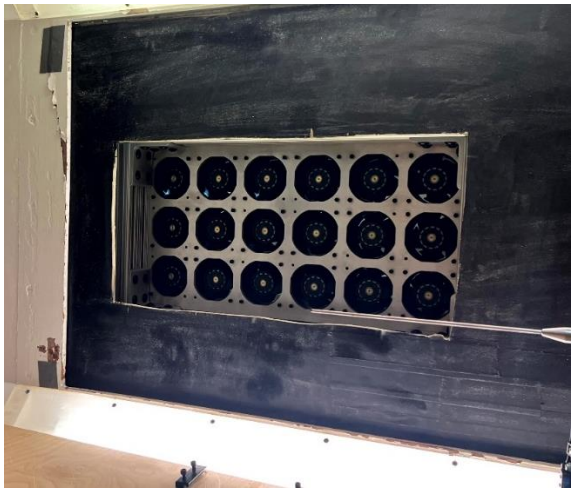

(c.)

Figure 3.7. (a.) Gust generator. (b.) Gust generator aligned with wind tunnel wall. (c.) Gust generator from inside the wind tunnel.

Coordinate Systems and Data Acquisition Grid Layout

In order to set a common, right-handed coordinate system frame of reference throughout the course of these experiments, a 3-D coordinate system was placed at the base of the rotor system, as shown in figure 3.8 below.

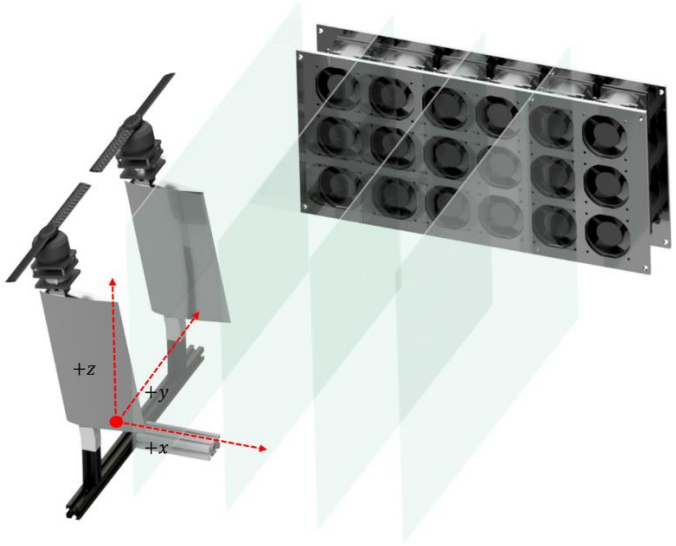

Figure 3.8. Coordinate system used in experiments, isometric view.

As shown in figure 3.8 , a 3-D cartesian frame was placed with an origin directly under the center of the inner rotor tips at the floor of the wind tunnel. As such in most air vehicle configurations, the positive x-axis extends parallel to the free stream flow, downstream, representing the longitudinal axis of the vehicle. The positive y-axis extends into the starboard lateral direction, and the positive z-axis extends into the positive vertical direction.

7-Hole Probe

The experimental setup for the 7-hole probe uses a rather simple, effective method for the collection of data in this experiment. With the primary goal of the project being to gain an understanding of the wake velocity distribution at different y-z planes, it was necessary to design a 3-D data acquisition grid that could be used for the 7-hole probe tests. To do this, a grid was constructed on the basis of four y-z planes at varying x locations. The figures below describes the layout of each 2-D grid, as well as their respective x (longitudinal) locations within the wake. It is important to note that all non-dimensional values are taken from the reference frames described in the section above. Also, figure 3.9a shows that the longitudinal distance between each plane is not equal throughout all four planes. This is due to wind tunnel restrictions, and these dimensions

are carried correctly through all results calculations. It is important to note that the crossflow generator is positioned in space in a way that does not affect the rotor's aerodynamic properties. That is, the crossflow generator is placed precisely where the physical "wake" of the rotors starts, and the crossflow does not impinge on or place the rotors into a sideslipping regime.

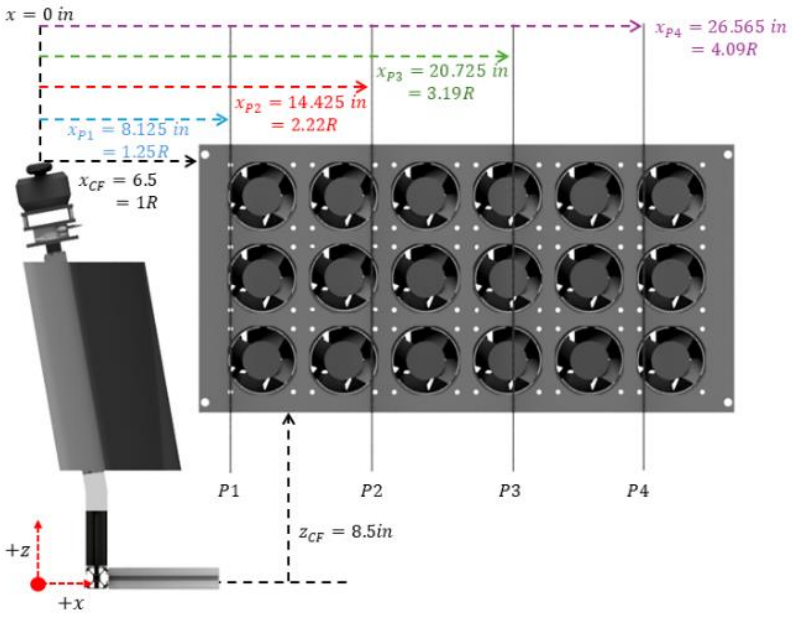

(a.)

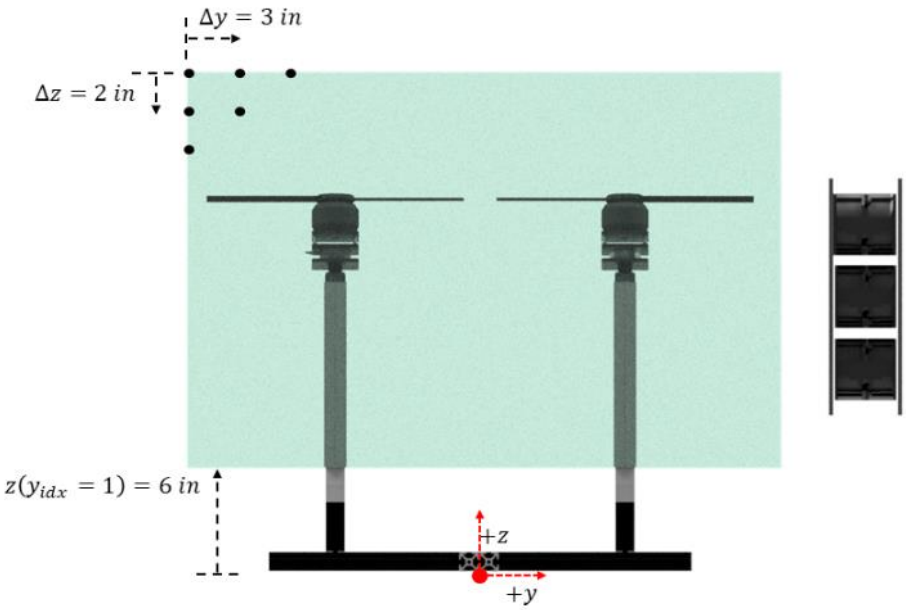

(b.)

Figure 3.9. Experimental configuration (a) Side view illustrating plane locations. (b) Rear view illustrating grid spacing.

The following figure shows a scatter plot of the grid itself with respect to the rotor rig.

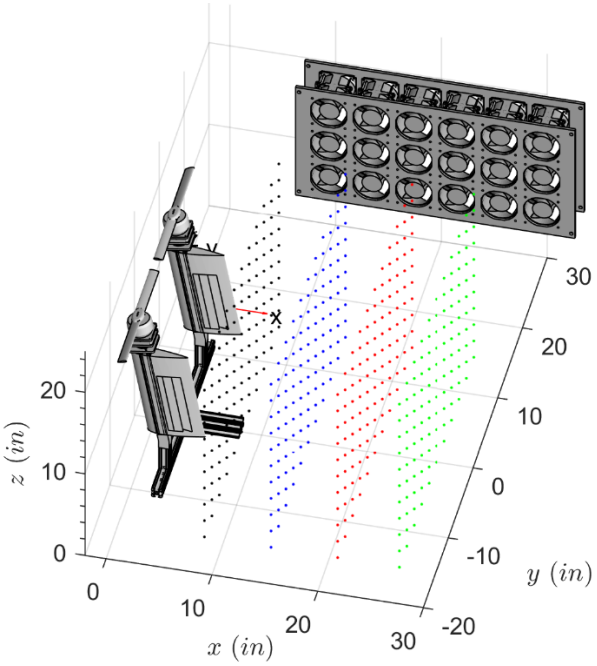

Figure 3.10. 7-Hole 3-D Grid.

As shown in figure 3.10 above, the grid sizing and fidelity was chosen by finding a balance between both the length of the test time and the coarseness of the grid. While it is important to have a fine grid for data interpretation and visualization, it is also important to be able to run the tests within a practical time limit. With this, the final grid used for all 7-hole probe testing was an 11x11 point grid on four separate longitudinal planes. The setup and control of the traverse system is explained in the next section.

To interface the probe with a computer, a high-speed USB-B to USB-A was used, and LabView was used to receive the 1000Hz raw pressure data, which will be discussed further in a following section.

The figures below show the 7-hole probe with the holder in the form of an initial CAD design, as well as the final 3-D printed part with the probe inserted. The mounting technique used to secure the sensor on the actuator system allows for the probe to be completely aligned with the freestream flow with zero incidence in any direction.

Figure 3.11. Probe and compression holder CAD.

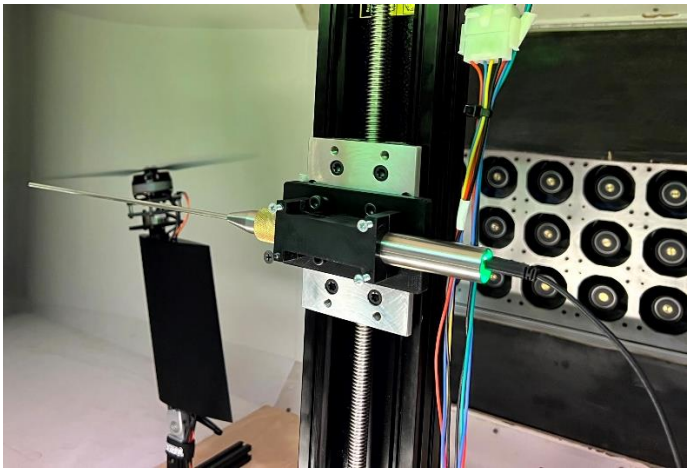

Figure 3.12. Full probe final rig assembly.

Traverse System

A 2-D traverse system was constructed and used for each of the chosen longitudinal locations of the wake. The traverse system specifications are outlined in table 3.2 below. Two high-precision Velmex actuators were used to traverse the 7-hole probe in the two directions of interest.

To meet the required grid locations as shown in figure 3.9b the following procedure was used to traverse the probe for each longitudinal test plane. This program was written into an Arduino script and implemented using stepper motor drivers and limit switches. More about the traverse sequence and grid can be found in the 7-hole and experimental procedure section.

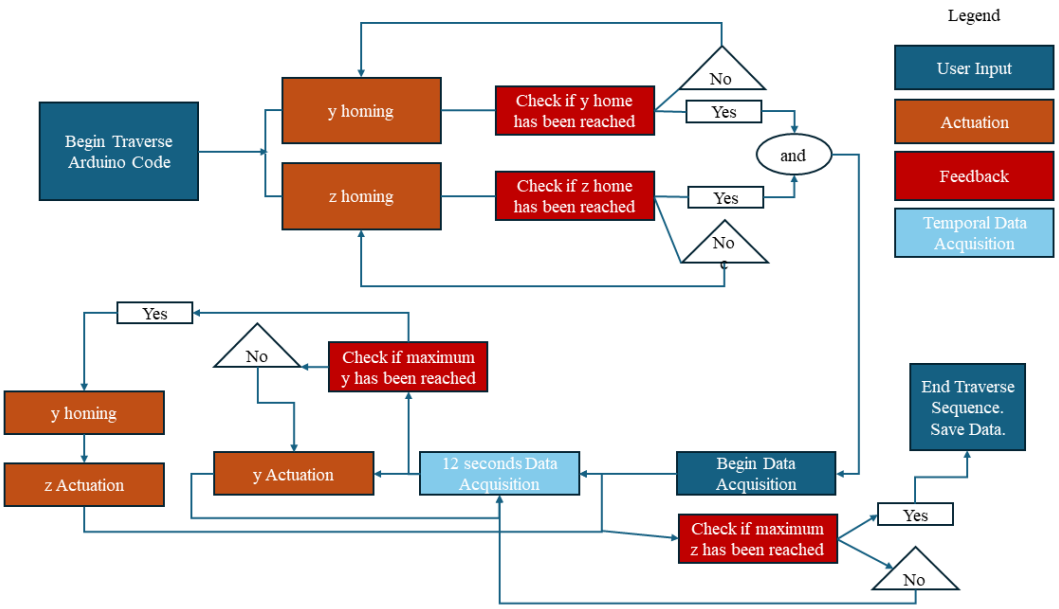

Figure 3.13. Traverse system control block diagram.

Electronics Configuration

The electronics configuration for the experiments presented in this thesis is centered, for the most part, around Arduino-based programs, with Matlab-based postprocessing. The following figure depicts the electronic configuration for 7-hole probe testing in the form of a block diagram.

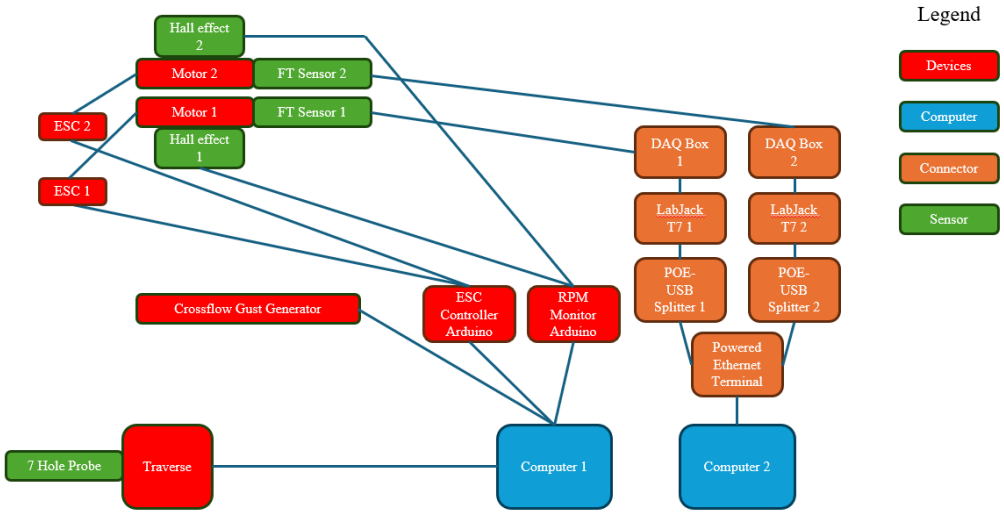

Figure 3.14. Electronics configuration block diagram.

To control RPM, two Arduinos Megas were used in parallel to maintain a constant RPM of 4000 for all experiments. Depending on flight condition (i.e. forward flight speed and rotor

selection), the motor ESC outputs were increased or decreased on one Arduino as needed to account for increased drag. On the second Arduino, the RPM was constantly monitored. It was found that by maintaining a constant ESC throttle on both motors, the RPM was able to stay at 4000rpm, with fluctuations of plus or minus 88 RPM for both rotor configurations. Each motor is equipped with a hall effect sensor as shown in the figure to achieve the RPM monitoring discussed.

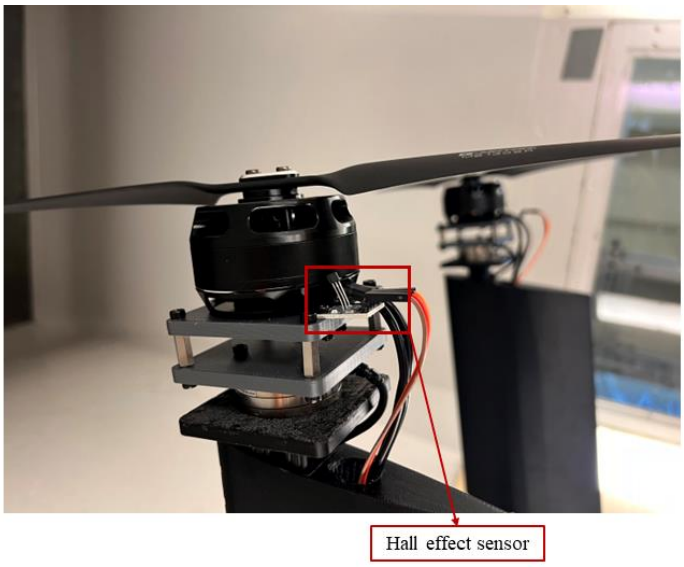

Figure 3.15. Hall effect sensor configuration.

Two 6-axis FT sensors are used to sense the forces each motor-rotor configuration produces. As shown in the block diagram in figure 3.14, the sensors are connected to data acquisition boards and subsequently to a computer via a series of ethernet cables and power over ethernet (PoE) splitters.

Complete Experimental Configuration

The following figure shows the complete experimental configuration for 7-hole probe testing.

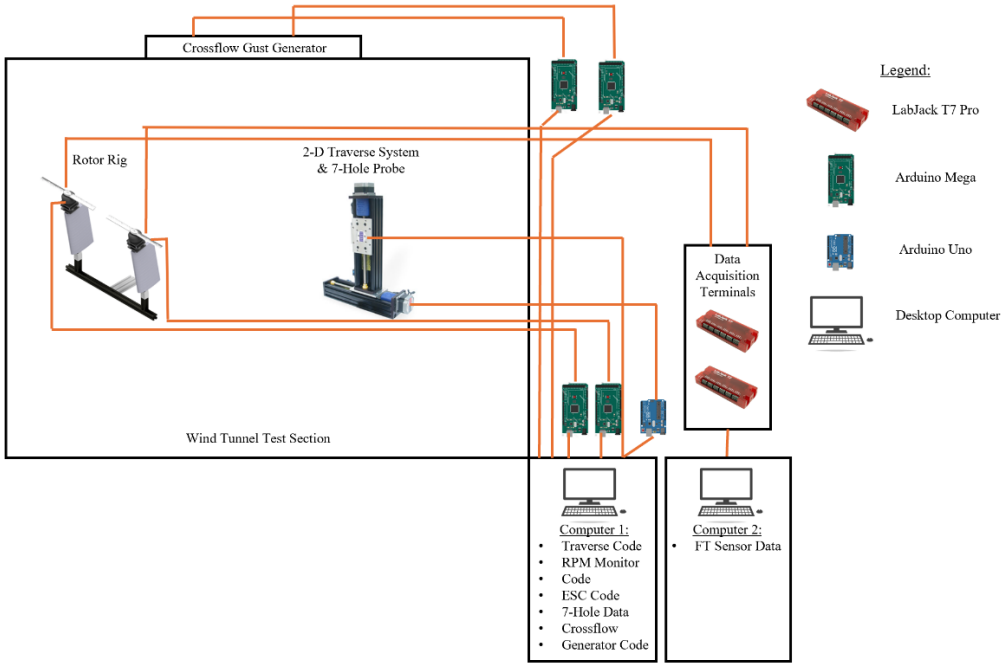

Figure 3.16. Rotor rig CAD rendering with component definitions.

The following table summarizes the specifications of each hardware item used in the experimental setup.

Table 3.2. Hardware used during experimentation.

Hardware Name	Specification/Model		Hardware Name	Specification/Model
Arduino	Mega (x4)		Data Acquisition Board (x2)	Labjack T7 Pro
Arduino	Uno (x1)		Force/Torque Sensor (x2)	ATI Industrial Automation Mini40
Motor (x2)	Tmotor U7 V2.0 420kV		7-hole probe	Surrey Sensors SN1051
ESC (x2)	Tmotor Flame 70A		Linear Actuator (y)	Bislide 30 inch
Stepper motor driver (x2)	EASON motor driver		Linear Actuator (z)	Bislide 20 inch
Hall effect sensor (x2)	HiLetgo sensor module			

CHAPTER 4. Experimental Procedure

Test Matrix

In order to successfully answer the open questions asked in the introduction section, a well-formulated test matrix is required. While creating a test matrix suitable for this project, the following aspects of experimental design were considered:

1. Encompassment of project objectives – will this test matrix allow us to answer the primary questions this project aims to solve?
    a. Both sets of rotors
    b. With or without crossflow
    c. Ambient turbulence measurements
    d. Various forward flight velocities
    e. Loads testing
2. Time of test – can these tests be completed with the small time windows of wind tunnel availability?
3. Amount of data – will the length of test allow for sufficient data processing and gathering of results?

With these aspects kept in mind, the following test matrix was constructed and completed for the project.

Table 4.1. Final performed test matrix.

Rotor Configuration	Crossflow
-	No
-	Yes
NACA	No
NACA	Yes
COTS	No
COTS	Yes

While table 4.1 above highlights all of the test's varying parameters, it is important to highlight fixed parameters within the experiments. Note that while the test matrix holds these parameters constant from test to test, actual values for some parameters may have offset from the planned values, and these are discussed in the results section.

It is important to note that the originally planned test matrix included multiple forward flight speeds. In order to find a balance between 1.) and 2.) in the above objectives, the goal of varying forward flight speed had to be taken out of the matrix for wind tunnel time constraints. Throughout this whole testing campaign (encompassing all of table 4.1) the wind tunnel was used for 30 hours, and the total testing duration was upwards of 120 hours.

Loads Testing

Loads testing was conducted using the ATI Mini40 6-axis force/torque sensors. Loads testing was completed with a simple method that included starting the rotors and wind tunnel to their required speeds, taking a minute of temporal loads data at 1kHz, and then averaging the results to get a single thrust coefficient for each flight condition.

7-Hole Probe Testing

The experimental procedure for retrieving 7-hole probe data involved a simple method that utilized the timing of the stepper motors located on the linear actuators, combined with Labview as the form of data acquisition for the experiment.

Firstly, the 2-D 11x11 grid was programmed into an Arudino script that follows the pattern presented in the block diagram in figure 3.13 Given the stepper motor's travel/revolution and steps per revolution, the steps to travel a certain distance (whether is be 3 inches horizontally or 2 inches vertically) can be calculated and input into the Arduino code.

Following the sequence presented in figure 3.13 the sequence can now be built into the Arduino script. To do this, a 12-second interval of time was allotted for each grid point for temporal velocity data to be taken. While the time allotted in the traverse sequence is 12 seconds, only 10 seconds of data are used during that time. The 2-second leeway is built in to make sure the effects of the actuator moving in the plane do not affect velocity data. From here, a traverse reset is built into the code in order to move the horizontal traverse back to the initial position. At this point, the vertical traverse increments up one (2 inch increment). The sequence repeats itself after this point until reaching the top z location. To understand the movements and timing of the actuator system in between each grid point, the movements were timed multiple times and averaged to get the exact travel time between each point within 0.01 seconds precision. With these timing values known, a Matlab script was written to parse out the raw pressure data from the probe. This script was checked for all 16 test planes to make sure the timing of each actuation aligns properly with the parsing function.

After the traverse system has been calibrated, the first tests could take place. The method of test, outlined in the steps below was used to perform the 7-hole tests.

1.) Open the LabVIEW file '7HP test panel.vi' (64-bit)
2.) Select the com port being used for the 7-hole probe.
3.) In 'command' click run self-test, run, and make sure all lights are green.
4.) In 'command' click 'set data rate'.
5.) In the 'data rate' tab, set the data rate to 1000hz.
6.) Go back to 'action' tab and run.
7.) Perform a permanent auto-zero for the probe.
    a. In 'command', select perform permanent auto zero before turning the gust generator on or wind tunnel on.
    b. The ΔP during this procedure must be equal to zero. This needs to be done before every test.
8.) In 'command' click 'get data rate' and run. Be sure the returned rate is 1kHz.
9.) Select finite samples.
    a. Change 'N samples' to 10000000000.
10.) In Windows, create the file you want to save the data for the plane in. Make sure the available space on the drive is 1 GB at least.
11.) In the GUI, select the filepath. Press the 'log data stream' button.
12.) Finally, in 'command' click 'Enable USB Streaming'
13.) At this point, the probe is ready for test. Begin the traverse sequence.
    a. The Arduino serial monitor will output a countdown once the traverse has been sent to the home position.
    b. It is imperative to start the 7-hole probe data acquisition as soon as the serial monitor tells you.
    c. While visually monitoring the test, let the sequence run for about 55 minutes.
14.) At the end of the sequence (y,z) = (30, 20) in, the traverse will move back to (y,z) = (0, 20). At this point, the 7-hole probe data acquisition can be stopped and the file can be saved.

All truth-airspeed measurements were taken from the wind tunnel dynamic pressure sensor, and they were cross-checked with an anemometer. It was found that the wind tunnel dynamic

pressure readout was within 2-3% of the anemometer reading. Because of this, the wind tunnel dynamic pressure sensor was deemed the true airspeed for all experiments. It is important to note that the dynamic pressure reading from the wind tunnel was taken before the rotors or crossflow gust generator were turned on. Due to the pressure/velocity effects of these experimental components, the dynamic pressure reading was altered by up to 0.1 psf after the ignition of these components. With this, all normalized values (for example, normalized velocity values) are normalized using that test's wind tunnel velocity from the dynamic pressure sensor.

Data Processing

To process 7-hole probe data, a suite of in-house-written Matlab processing scripts and functions were used. The general step-by-step process for processing a full set of four planes of 7-hole data is outlined below. After retrieving the four ~55-minute raw pressure data files,

1.) Run the function 'Parse_data.m' (see appendix A.) for each plane's raw pressure data file. This function splits the raw data file in an 11x11 cell array, which contains the full temporal pressure matrix to be used in a future step.
2.) Save this .mat file in the same directory as the active Matlab filepath.
3.) Using the specific probe's calibration file, 'SN1051.xlsx', run 'Seven_Hole_Processing_Joseph.m' (see appendix B.) for each saved planar temporal pressure data. This function assumes four planes are being used, therefore there are 4 cell array file inputs hardcoded within the script. The function then employs Bernoulli's equation in 3 dimensions to output the velocities u, v, and w at each grid location. Outputs are stored in a structure, which contains lower-level branches of Plane1, Plane2, Plane3, and Plane4, which each contain a cell array of time, u, v, and w for each grid point.
4.) To postprocess the output structure of 'Seven_Hole_Processing_Joseph.m', the script 'Post_Processor.m' can be used. This function goes through a plethora of various mean velocity calculations and turbulence processing parameter calculations. A complete list of the parameters processed in this code is outlined in the list below, and the methods of postprocessing techniques are discussed for relevant parameters in the results section.

u, v, w	u', v', w'	$\lvert\vec{V}\rvert$	U_{mean}	I
u_{rms}	TKE	$\tau_u,\ \tau_v, \tau_w$	$u'u', v'v', w'w'$	$u'v', u'w', v'w'$

CHAPTER 5. Results

Preface

In an effort to declutter results figures, the following convention will be used to mark locations of rotors in all 2-D contour plot figures:

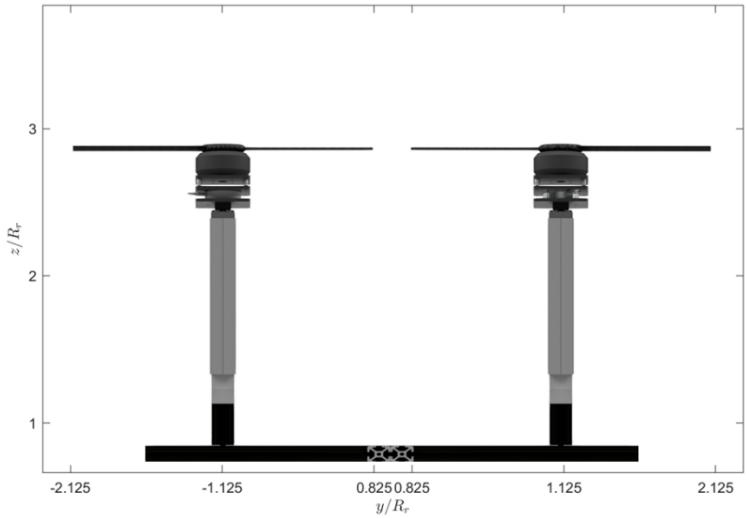

Figure 5.1. Rotor location convention used for all contour plots.

It is important to note the location of the rotors within the 2-D plane. The lateral locations of the rotor tips and hubs, as well as the vertical location of the rotor remain constant and independent of other factors throughout all result figures unless otherwise specified. All contour plots are viewing the plane in question from the backside or the rotor rig. In other words, the reader is viewing the plot looking into the negative x-axis space.

Day-of Test Conditions

All tests, regardless of tests with or without rotors, were run at a wind tunnel dynamic pressure 1.01 psf, which equates to a V_∞ or forward flight velocity of 29.1 ft/s. With this, the tip Reynolds number for experiments with rotors be calculated using equation 8.

$$Re_{tip} = V_{\text{tip}} c_{tip} / \nu \tag{8}$$

This Reynolds number is calculated on the advancing side of the rotor at the fastest azimuth angle location relative to the laboratory frame. The chord is calculated based on the tip chord of either rotor in question, based on values shown in table 5.1. In equation 8, it is important to note that V_{tip} includes the tip speed due to angular rotation, as well as the tip speed due to forward flight, given by equation 9.

$$V_{tip} = V_\infty + \Omega R_r \tag{9}$$

The tip Mach number can be calculated using equation 10, and it was found in order to show the extent to which this experiment involves compressible flow.

$$M_{tip} = V_{tip}/a \tag{10}$$

As shown in table 5.1, all tip Mach numbers were under Mach 0.3, which means the flow is almost completely incompressible and the effects of compressibility can be ignored.

With equations 8 - 10, the advance ratio given α_{plr}, Ω, V_{tip} and R_r can be found using equation 7. The calculated rotor tip speeds, tip Reynolds numbers, tip Mach numbers, and advance ratios for both rotors are shown in table 5.1.

Table 5.1. Rotor aerodynamic test parameters.

Parameter	Rotor A (COTS)	Rotor B (NACA)
V_{tip}	256.01 ± 18.33 ft/s	256.01 ± 18.33 ft/s
M_{tip}	0.227 ± 0.016	0.227 ± 0.016
μ	0.126 ± 0.00292	0.126 ± 0.00292
Re_{tip}	79,000 ± 6,000	114,000 ± 8,000
$C_{T,hover}$	0.0098	0.0041
$C_{T,Forward\ Flight}$	0.0150	0.0050

Results from the calculations presented in table 5.1 show that the flow at the critical Mach location (rotor tips) is highly incompressible, and the Reynolds number is moderately low for both rotor cases.

An important experimental defect was observed during some of the tests and accounted for in the form of a correction in the post-processing script. During all tests, it was observed that the 7-hole probe was tilted slightly downwards in the vertical axis for planes 3 and 4. Because of this, a function was implemented to back out this angular error, based off the figure below.

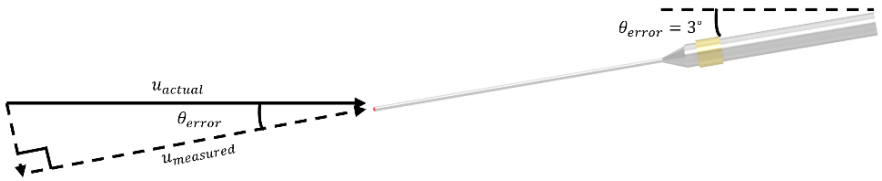

Figure 5.2. Resolution effort for -3° 7-hole probe tilt recognized in planes 3 and 4.

With this, the following equation was used to resolve the true velocity component in the longitudinal (x) direction.

$$u_{actual} = \frac{u_{measured}}{\cos(3°)} \tag{11}$$

Previous experimental campaigns in NCSU's subsonic wind tunnel have noted that a drastic rise in internal static temperature is likely to occur over long-duration tests. This parameter was monitored carefully throughout the duration of our tests. It was found that all tests stayed under 80°F for the entirety of the test. As previously mentioned, the duration of each test is approximately 55 minutes, therefore it was important to monitor the change in conditions over the test interval in order to obtain a plane's data that can be accurately correlated to each other. With this, it was found that the static temperature within the wind tunnel varied no more than 6°F for any given test. While this value is rather small, for the accuracy of results, the 7-hole data processor takes into account the change in temperature over the course of the test when computing velocities within each plane.

Wind Tunnel Ambients

To gain an understanding of the freestream flow conditions and ambient turbulence within the wind tunnel, an extensive study was completed without the rotor rig installed in the wind tunnel. Firstly, a study was completed on solely the wind tunnel (which represents the forward-flight freestream). As previously discussed, all wind tunnel tests were completed with a tunnel pitot-tube dynamic pressure (taken before crossflow or rotors are turned on) of 1.01psf, which equates to a freestream velocity of 29.1ft/s.

The point-averaged velocity contour results, normalized by the freestream velocity U_∞ of this test for each plane are shown in figure 5.3 below.

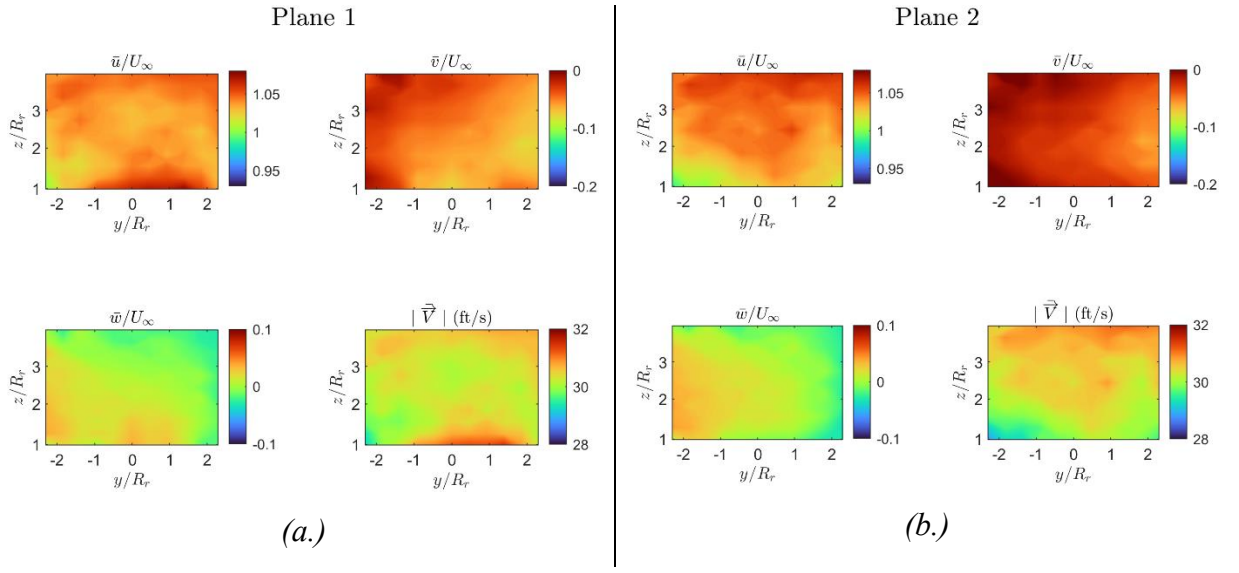

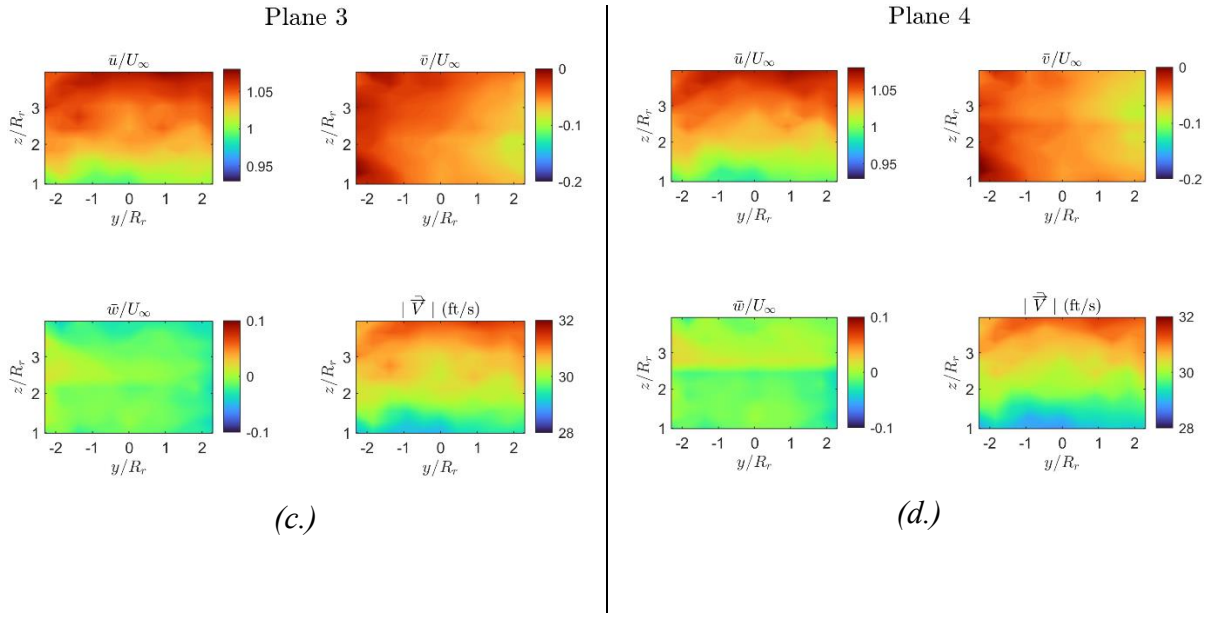

Figure 5.3. Wind tunnel velocity contours (a.) Plane 1. (b.) Plane 2 (c.) Plane 3 (d.) Plane 4.

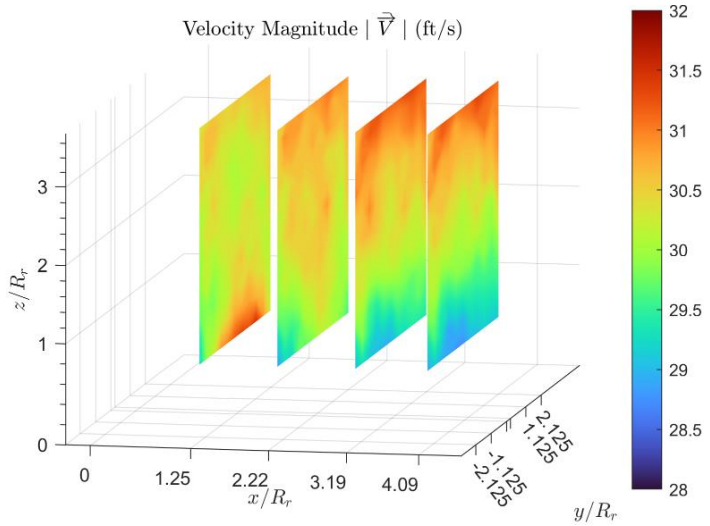

Figure 5.4. Wind tunnel ambient velocity magnitude plots, isometric view.

From figures 5.3 and 5.4, it was found that the flow is decently uniform over the whole test section. It was found that, compared to the calculated freestream velocity from the wind tunnel airspeed sensor, there are areas of velocity surplus in the upper z regions of the test section, while there are regions of velocity deficit in the lower z regions of the test section. This is primarily evident in further downstream planes.

To investigate these surpluses, deficits, and fluctuations further, turbulence intensity can be calculated from the time-history raw velocity data. For each grid locations' 10-second temporal velocity data, the turbulence intensity was calculated as follows:

After calculating the average velocities ($\bar{u}$, $\bar{v}$, $\bar{w}$) at each point, the temporal fluctuation can be calculated for each grid point using equation 12. It is important to note that the following calculations are completed in all three dimensions.

$$u' = u - \bar{u} \tag{12}$$

For each grid location and every timestep, the temporal variance is calculated as in equation 13.

$$(u')^2 = \begin{bmatrix} u'(t=0) \\ u'(t=1) \\ u'(t=2) \end{bmatrix} \cdot \begin{bmatrix} u'(t=0) \\ u'(t=1) \\ u'(t=2) \end{bmatrix} \tag{13}$$

The average of the temporal variance is taken for each grid point, resulting in $\overline{u'^2}$

With the three variance averages, the root mean square velocity (RMS) is determined for each grid point using equation 14.

$$u_{rms} = \sqrt{\frac{1}{3}\left(\overline{u'^2} + \overline{v'^2} + \overline{w'^2}\right)} \tag{14}$$

Finally, turbulence intensity (I), can be calculated using equation 15.

$$I = \frac{u_{rms}}{|\vec{V}|} = \frac{\sqrt{\frac{1}{3}\left(\overline{u'^2} + \overline{v'^2} + \overline{w'^2}\right)}}{\sqrt{\bar{u}^2 + \bar{v}^2 + \bar{w}^2}} \tag{15}$$

The turbulence intensity results for this study are shown in figures 5.5 and 5.6 below.

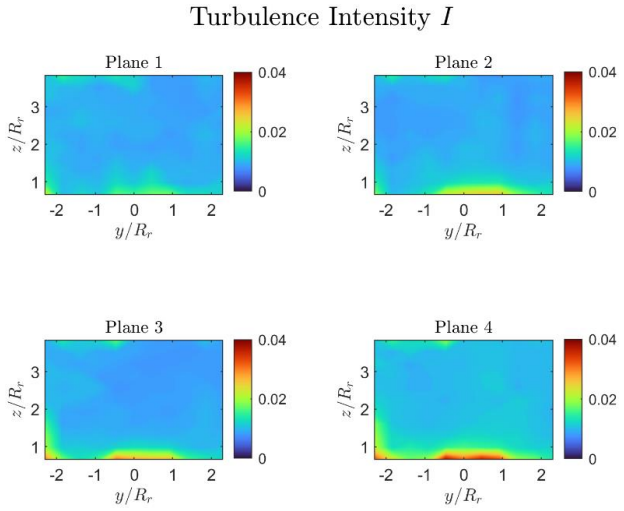

Figure 5.5. Wind tunnel ambient turbulence intensity contours at each plane.

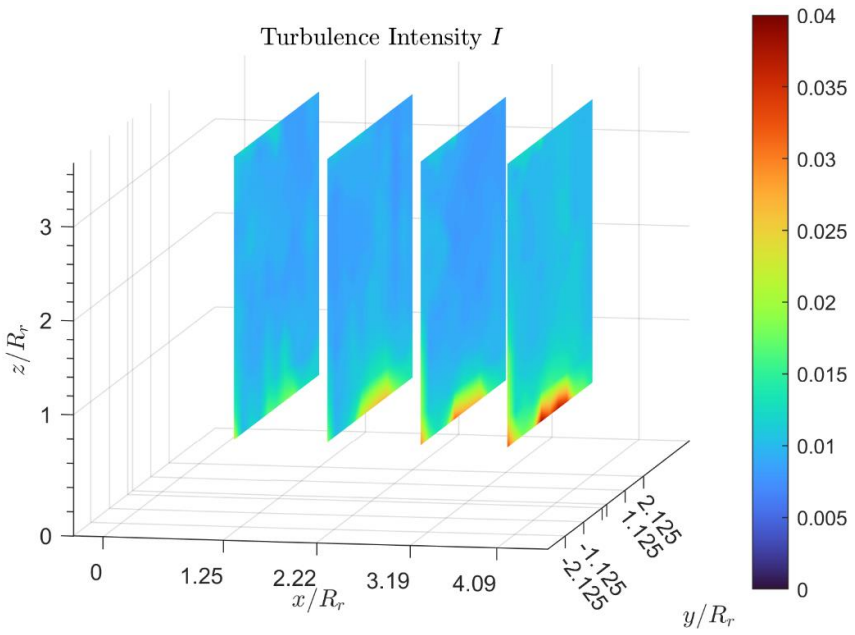

Figure 5.6. Wind tunnel ambient turbulence intensity plots, isometric view.

As shown in figures 5.5 and 5.6 above, there is an interesting phenomenon that was observed in progressively further downstream planes. This phenomenon is a hotspot of turbulence intensity on the lower parts of plane 4, which builds up gradually from the front of the test section. I have deduced this occurrence to be a shear layer build-up coming from the test stand base, which was inside of the tunnel at $x = 1\,in$ during the wind tunnel ambient tests. The difference in turbulence intensity within this shear layer is only approximately 3% as compared to the bulk flow within plane 4. It was also found in subsequent tests than turbulence from the base of the test stand does not impinge on the wake of the rotors.

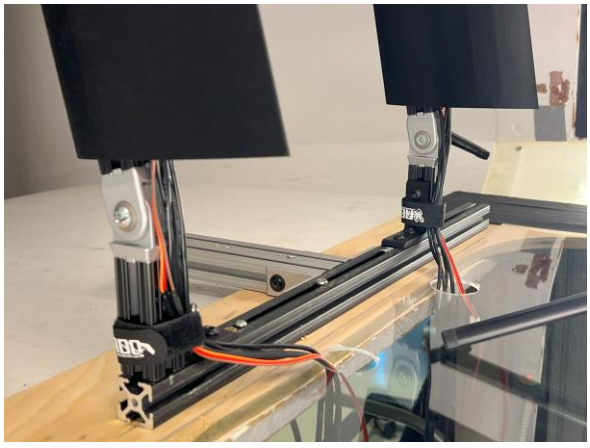

Figure 5.7. Test stand base.

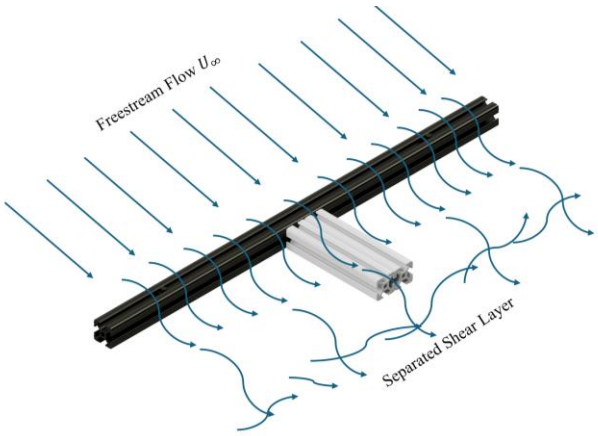

Figure 5.8. Shear layer buildup over test stand base visual.

Wind Tunnel with Crossflow Ambients

For all tests with crossflow gust, the PWM frequency sent to the gust generator fans was set to 0.5 uniformly across the entire 3x6 fan array. As shown in the test matrix, using an anemometer, the perpendicular gust speed was found to be 15 ft/s at the center lateral position of the wind tunnel ($y = 0$).

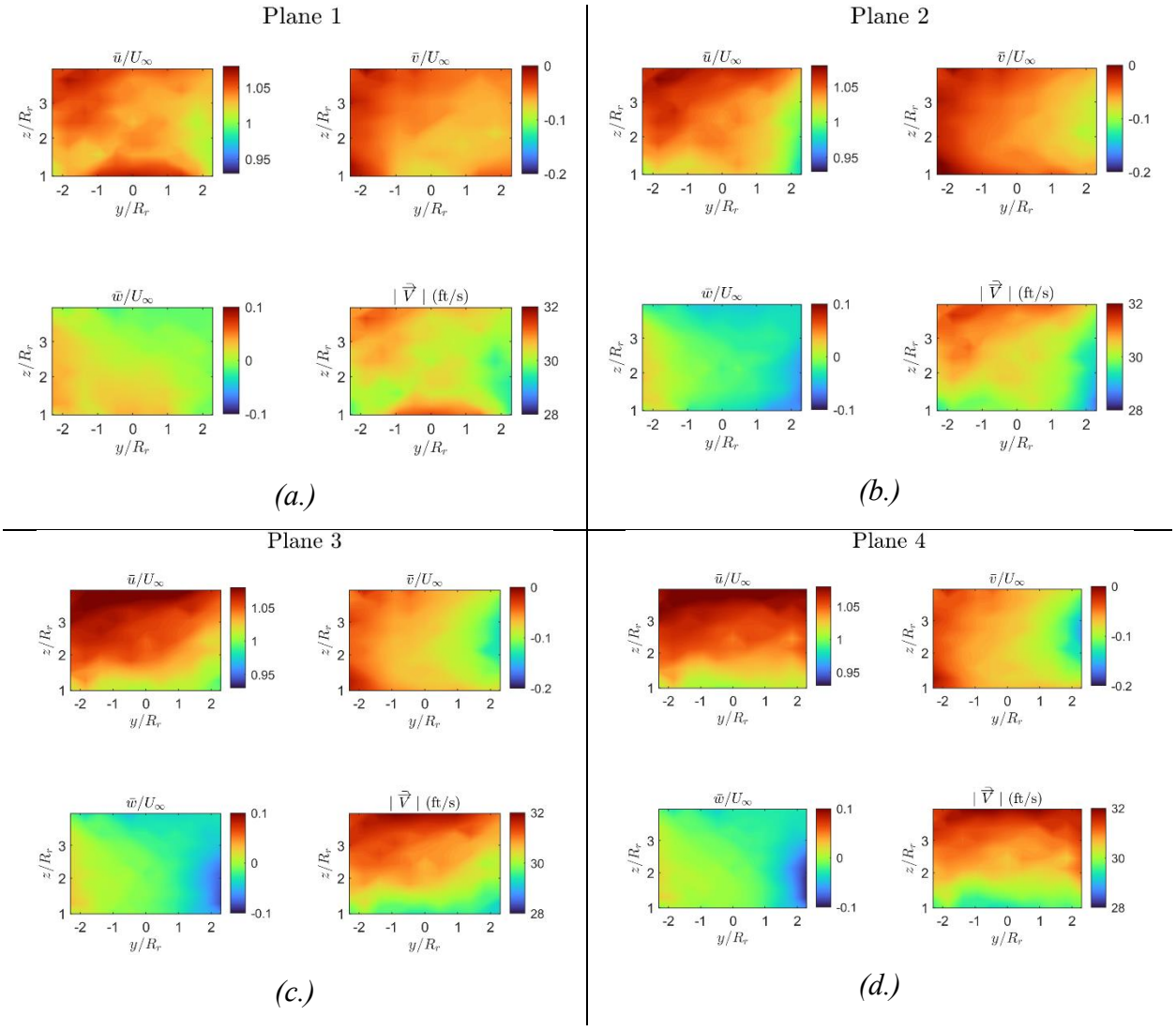

Figure 5.9. Wind tunnel with crossflow gust applied ambient velocity contours (a.) Plane 1. (b.) Plane 2 (c.) Plane 3 (d.) Plane 4.

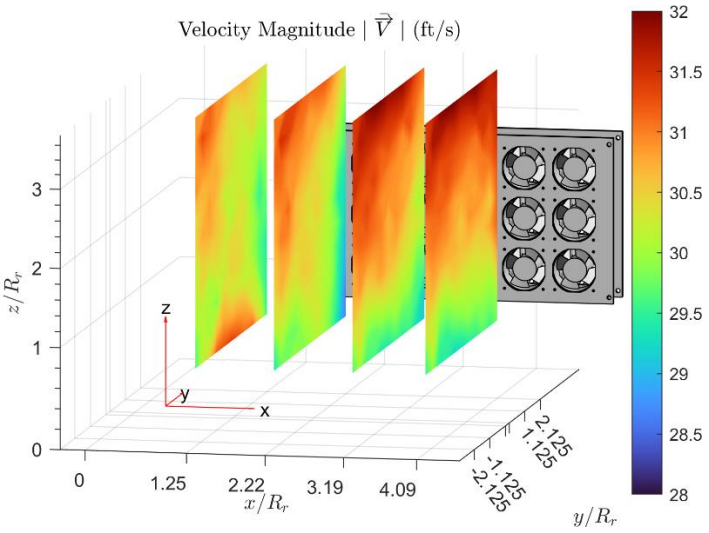

Figure 5.10. Wind tunnel with crossflow gust applied ambient isometric velocity magnitude contour plots.

As seen in figures 5.9 and 5.10, there are many similarities in the flow characteristics with crossflow as it relates to wind tunnel flow without crossflow. The average velocity in the longitudinal direction is still very close to the wind tunnel dynamic pressure sensor reading, and similar regions of velocity deficits and surpluses are relevant within this analysis.

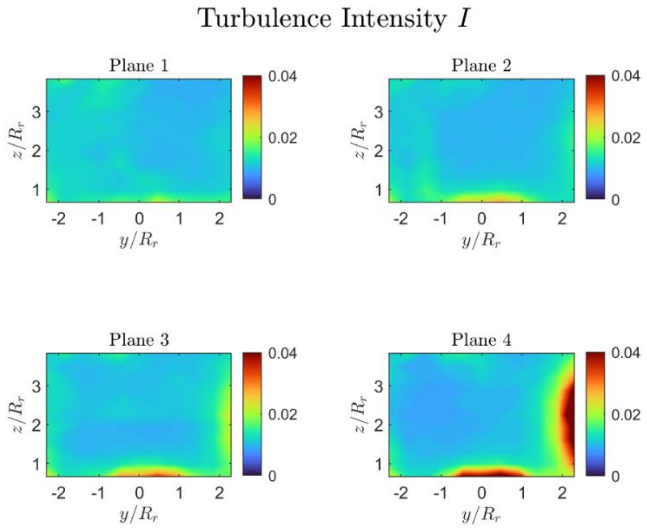

Figure 5.11. Wind tunnel ambient turbulence intensity contours at each plane.

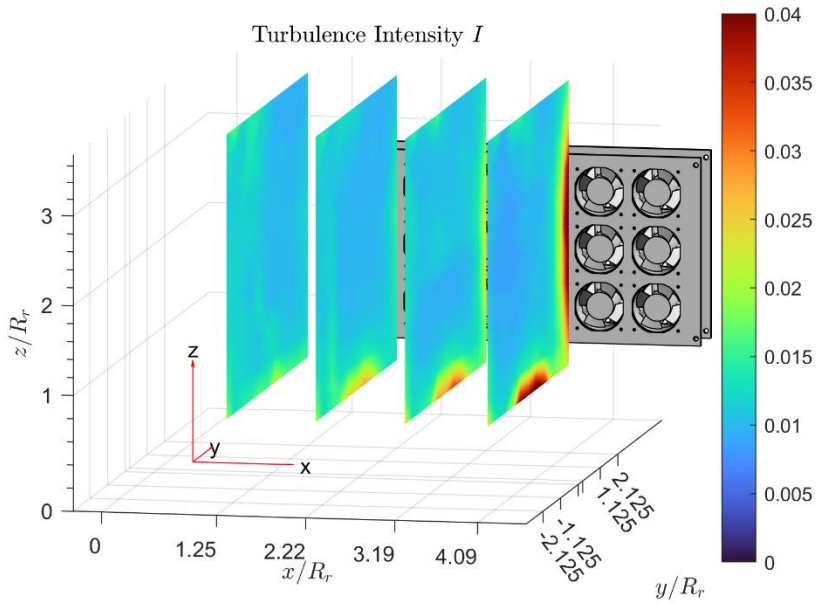

Figure 5.12. Wind tunnel ambient turbulence intensity plots, isometric view.

From a turbulence intensity perspective, the crossflow gust generator adds a region of heightened turbulence intensity that is primarily relevant in the downstream planes. Being as the gust generator begins to act on the flow just after plane 1, it was found that the turbulence within the crossflow gust grows as more fans continue to act on the flow. It was found that, at plane 1, the turbulence within the testing domain is essentially equivalent to the freestream turbulence. Throughout the ~0.0559 seconds of crossflow impingement on the freestream, the turbulence intensity builds up to a maximum value of 4.00 ±.01% . These results show that the primary effects of crossflow on freestream turbulence are present only on the outermost positive y regions of the domain. Relating this back to figure 5.9 (a. – d.) lateral velocity distributions (v/R_r) for each plane, it can be deduced that heightened turbulence intensity is present in regions of higher lateral (or crossflow) velocities. At lateral locations closer to the origin (or center of the testing domain), this lateral velocity is still present but is much lower, and the turbulence intensity behavior follows the same trend. The fall-off of turbulence intensity produced by the crossflow gust generator is more rapid with the freestream wind tunnel flow impingement.

Multirotor Wake Test Results: COTS Configuration

The first multirotor wake tests involved the use of the COTS rotor configuration. As discussed earlier, all tests were conducted with the rotors placed with a separation distance of $S/R_r = 0.25$. The 2-D contour plotting convention with rotors follows figure 5.1.

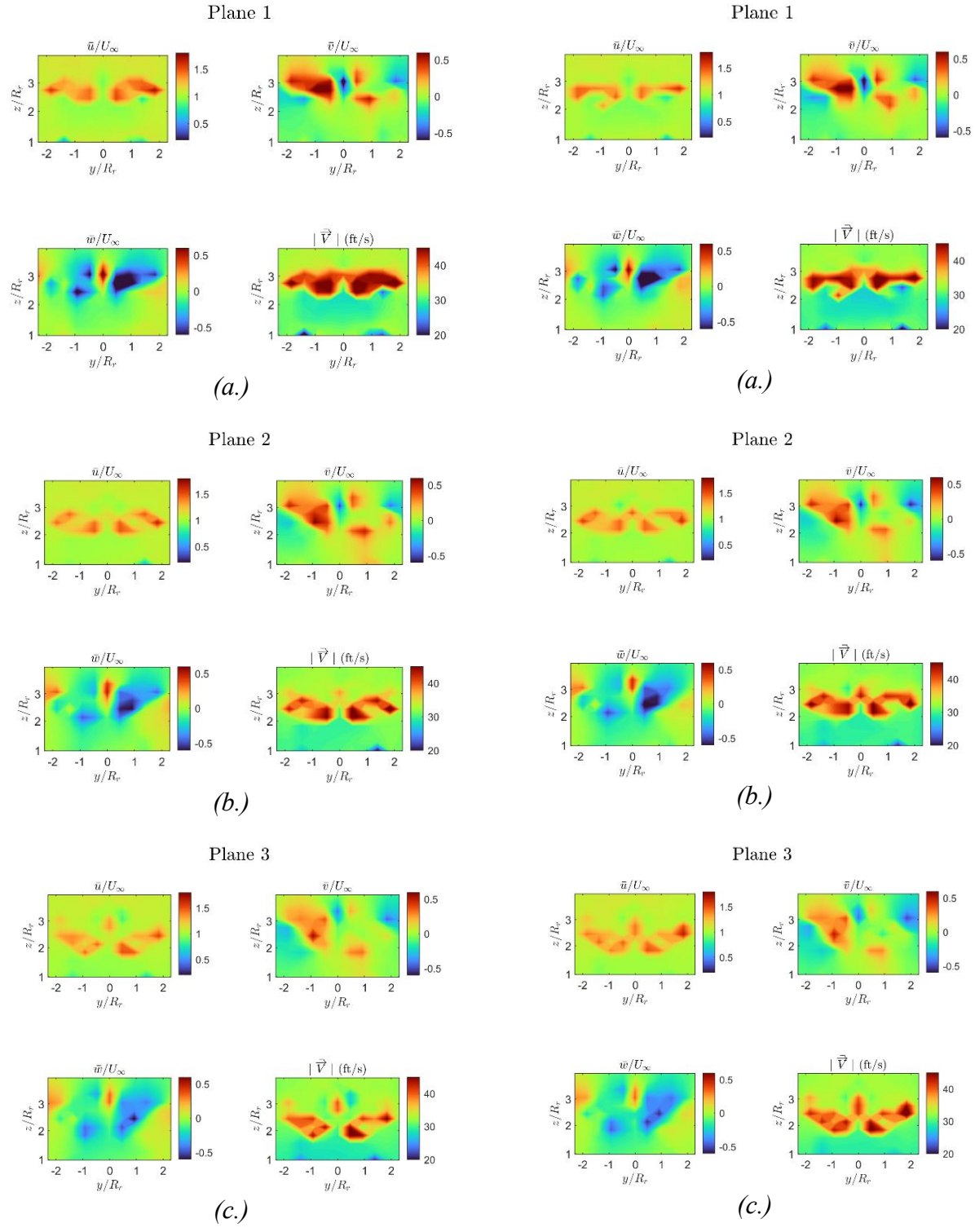

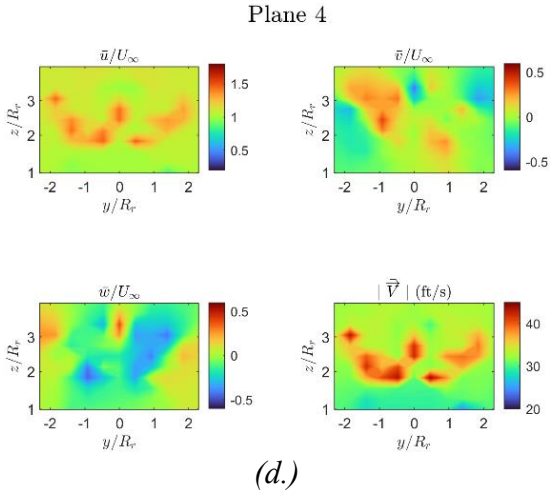

Figure 5.13. COTS rotors without crossflow planar velocity contours. (a.) Plane 1. (b.) Plane 2 (c.) Plane 3 (d.) Plane 4.

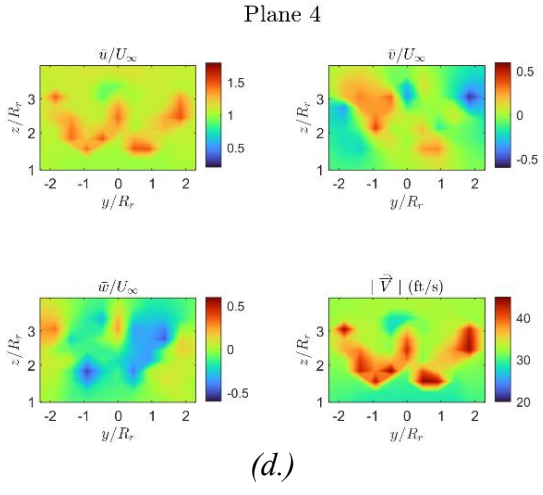

Figure 5.14. COTS rotors with crossflow planar velocity contours. (a.) Plane 1. (b.) Plane 2 (c.) Plane 3 (d.) Plane 4.

Figures 5.13 and 5.14 tell a great story about how the COTS rotor wake behaves in both with and without the presence of crossflow gust. The following figures show the combined velocity magnitude plots in figures 5.13 and 5.14 (bottom right tile) to provide the reader with more of a 3-D visualization of what is happening in the wake of the rotors.

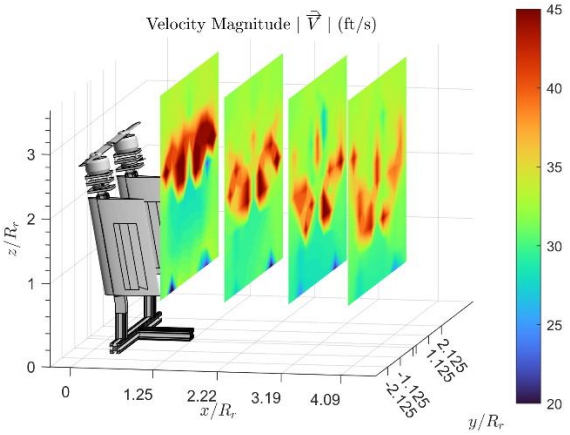

Figure 5.15. COTS rotors without crossflow isometric velocity magnitude contours.

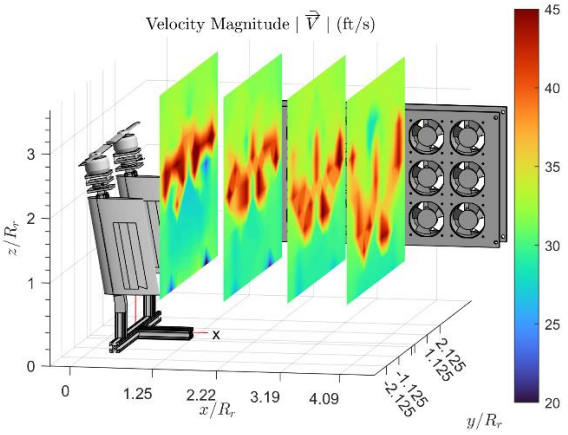

Figure 5.16. COTS rotors with crossflow isometric velocity magnitude contours.

After surveying the flow within each plane in the wake, very defined velocity deficits and surpluses were easily noticeable from the velocity contours. Surpluses as high as 160% of the freestream velocity were found within the slipstream boundary areas near the tips of the rotors. The highest velocity surpluses were found within pane 1, which is as expected and hypothesized. It was also found that, as expected, the general slipstream body propagates downward in furthering

downstream plane locations. In both cases of without and with crossflow, both rotors' vertical tip vortex locations moved by nearly $2z/R_r$ throughout the length of the testing domain. This will be discussed more in a later section. Laterally, it was found that the advancing side of each rotor experienced drastically higher velocity surpluses, which is congruent with aerodynamic principles that a wing moving with a higher airspeed will produce more lift than the same wing moving with a lower airspeed.

Interestingly, it was found that there were no major velocity deficits found in the u or $|\vec{V}|$ speed contours. However, v and w deficits and surpluses were all experienced within tip vortex locations. For example, in figure 5.13 and 5.14, high shears in the negative z direction were found in all regions of the slipstream. With increasing downstream planes, the location of these vertical shears moved downwards in the negative z direction, which is congruent with equations 4-6. For grid locations where the velocity probe in implanted in a tip vortex, it was found that the highest surpluses and shears are in the negative y direction. While this can be said about the flow at this specific point, it is not feasible to say that the overall shear direction within all tip vortices is in the negative y direction; it is only true for this specific point which may or may not be on the upper side of a vortex core.

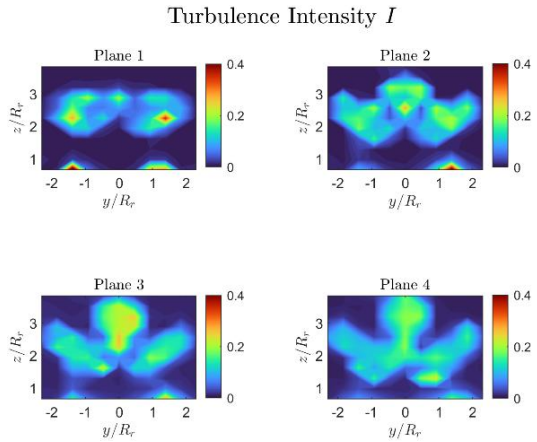

(a.)

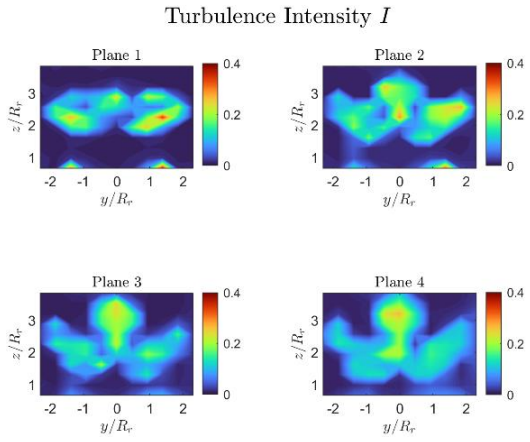

(a.)

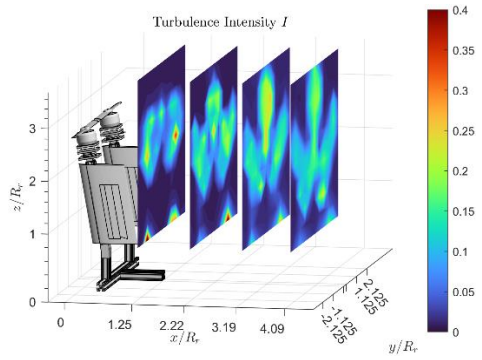

(b.)

Figure 5.17. COTS rotors <u>without</u> crossflow turbulence intensity contours. (a.) Planes 1-4 (b.) Isometric view.

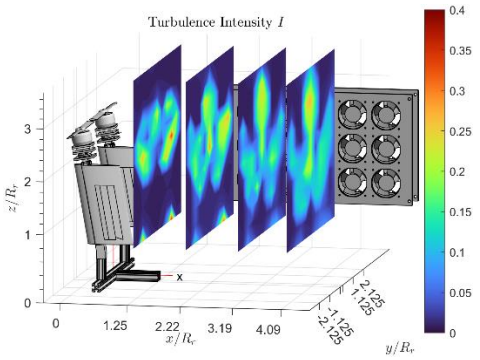

(b.)

Figure 5.18. COTS rotors <u>with</u> crossflow turbulence intensity contours. (a.) Planes 1-4 (b.) Isometric view.

The plots of turbulence intensity produced very interesting results for all test cases with rotors. As expected, all tip vortex locations (for example, $\left(\frac{y}{R_r}, \frac{z}{R_r}\right) = (-1.5,\ 2.1)$ in plane 1, or $\left(\frac{y}{R_r}, \frac{z}{R_r}\right) = (0.75, 1.5)$ in plane 4) show incredibly heightened turbulence intensity values. Values in these locations were as much as 40% higher than that of other locations within the flow. In both the case of without (figure 5.17) and with (figure 5.18) crossflow, a phenomenon occurred in between the rotors, where turbulence intensity increased with increasing downstream location. For example, in both figures 5.17 and 5.18, there is a relatively low turbulence intensity in between the rotor tips in plane 1, but the downstream planes all have buildups of turbulence intensity present. The likely reason for this is a conglomerating recirculation of flow in these regions. Relating these results back to figures 5.13 and 5.14, there are heightened vertical and horizontal shears in these locations and their respective planes.

Multirotor Wake Test Results: NACA Configuration

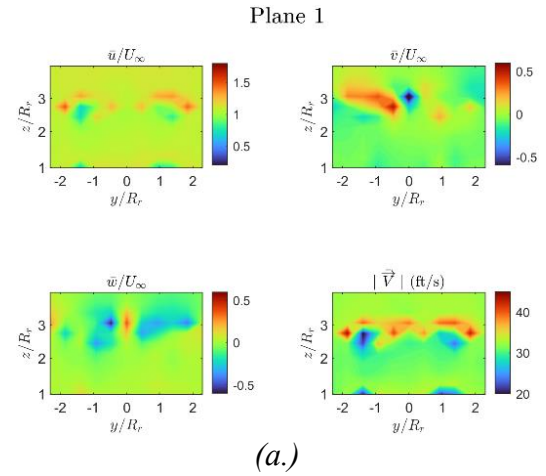

(a.)

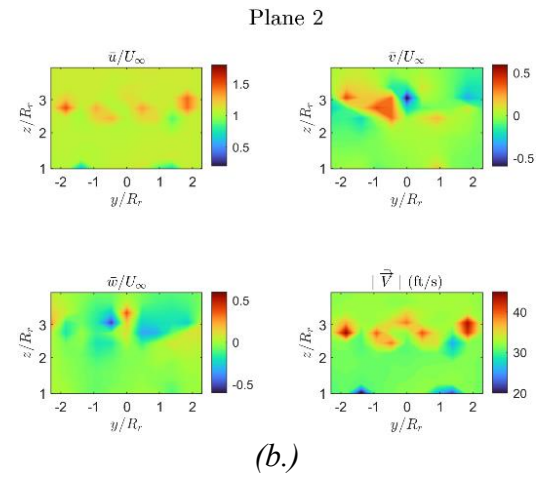

(b.)

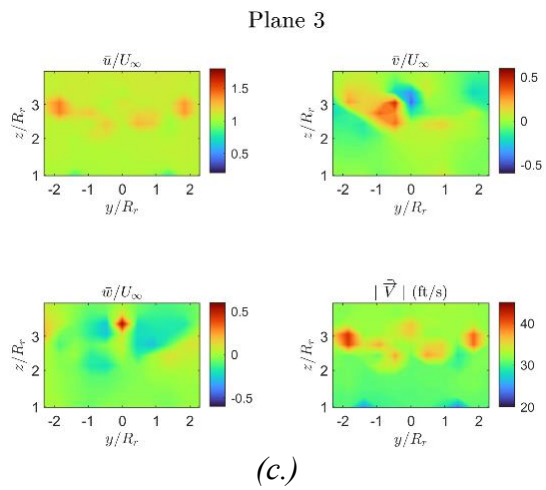

(c.)

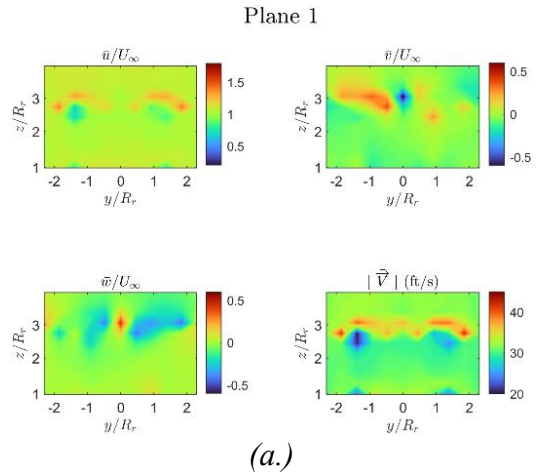

(a.)

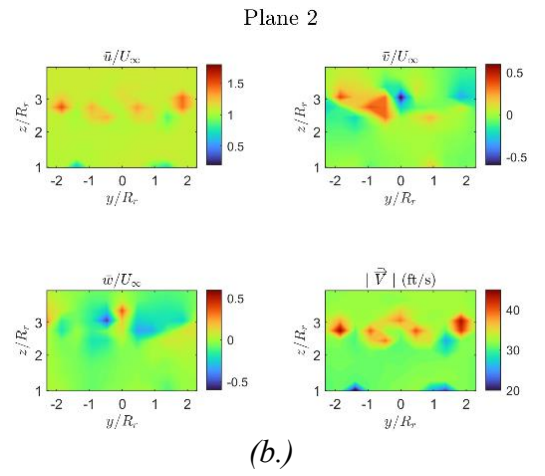

(b.)

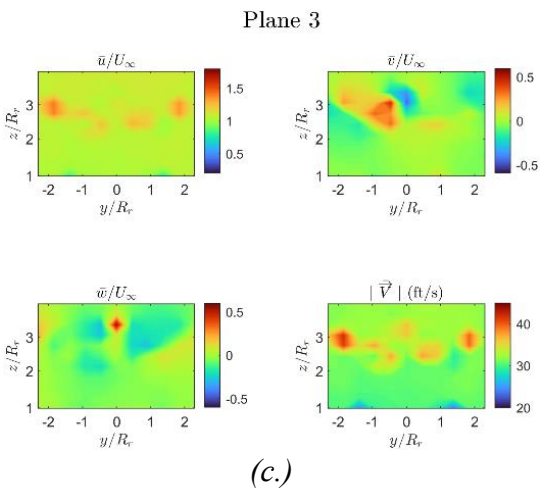

(c.)

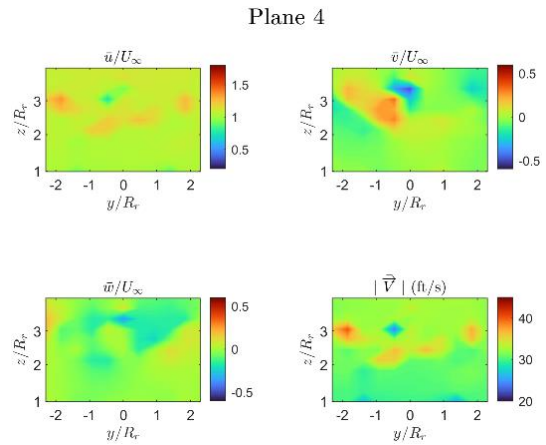

(d.)

Figure 5.19. NACA rotors without crossflow planar velocity contours. (a.) Plane 1. (b.) Plane 2 (c.) Plane 3 (d.) Plane 4.

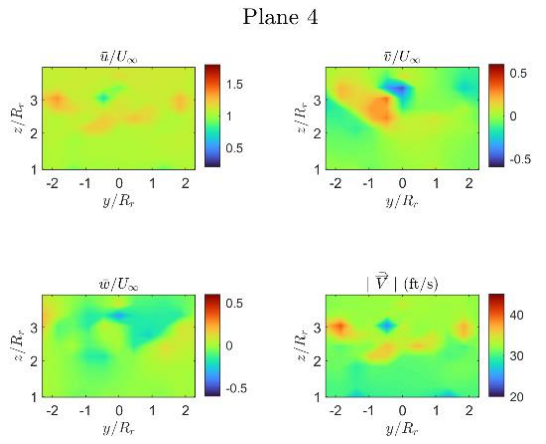

(d.)

Figure 5.20. NACA rotors with crossflow planar velocity contours. (a.) Plane 1. (b.) Plane 2 (c.) Plane 3 (d.) Plane 4.

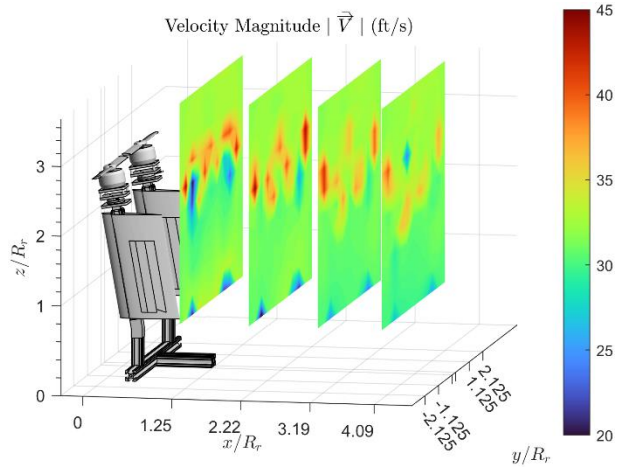

Figure 5.21. NACA rotors without crossflow isometric velocity magnitude contours.

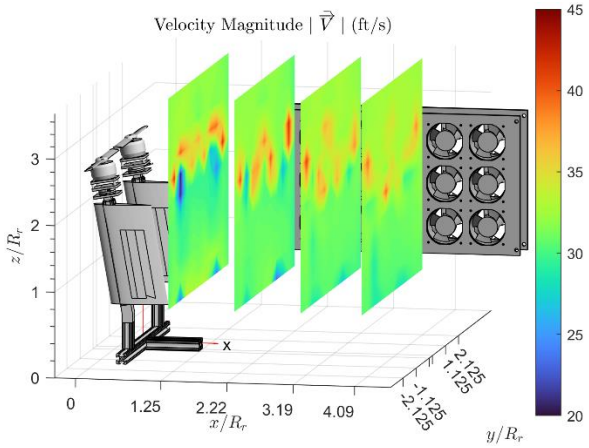

Figure 5.22. NACA rotors with crossflow isometric velocity magnitude contours.

The results of without crossflow and with crossflow tests in the NACA configuration are very similar to the COTS configuration, with the primary differences being in the velocity deficit and surplus profiles. Overall, the NACA rotor configuration produced significantly lower velocity surpluses and higher velocity deficits than those of the COTS configuration. These findings are congruent with the findings of lower thrust coefficients with the COTS rotors, which will be discussed in a later section.

Similarly to the COTS configuration results, vertical and lateral wind shears were found to be significantly (~40%) higher or lower in plane 1 as compared to the same location in plane 4.

With crossflow, it is visually easy to see that wind shears decreased more quickly in downstream planes than in the without-crossflow cases. This will be analyzed more in figures 5.26 and 5.27.

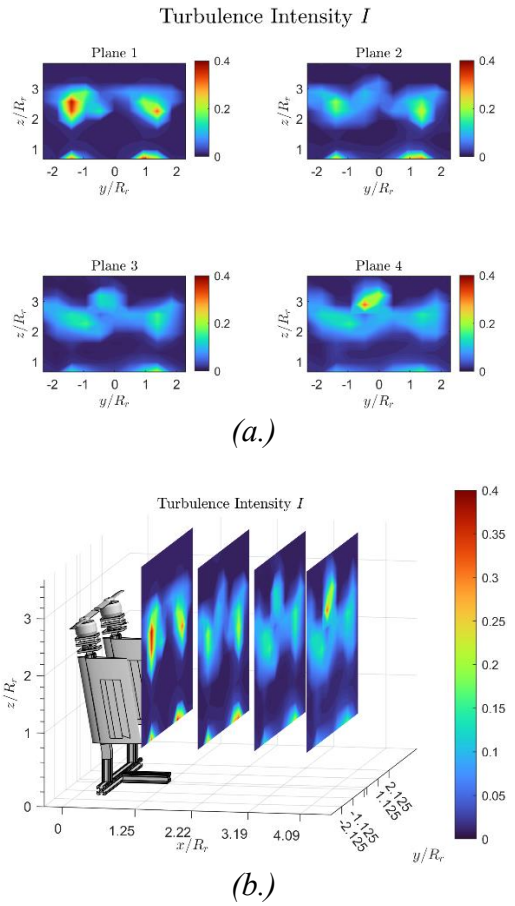

Figure 5.23. NACA rotors <u>without</u> crossflow turbulence intensity contours. (a.) Planes 1-4 (b.) Isometric view.

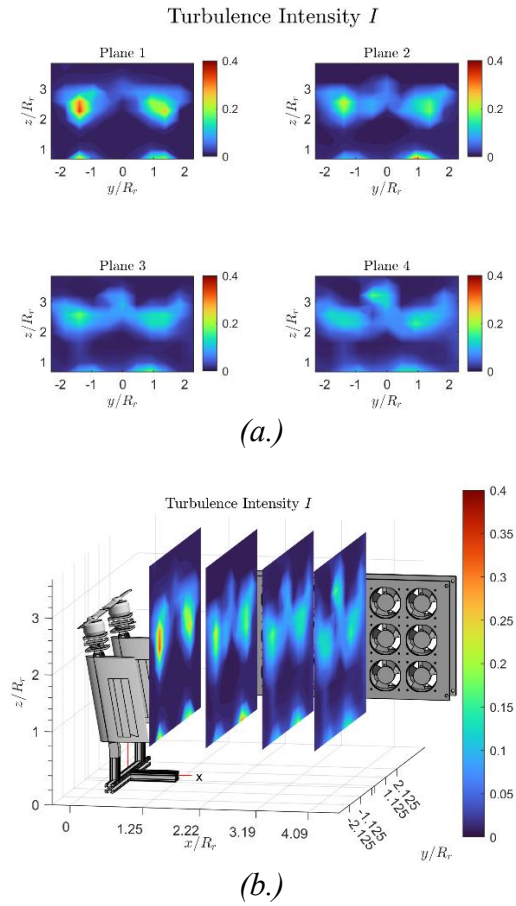

Figure 5.24. NACA rotors <u>with</u> crossflow turbulence intensity contours. (a.) Planes 1-4 (b.) Isometric view.

Overall, turbulence intensity plots exhibited similar behaviors to the behaviors exhibited in the COTS configuration. The most intense locations existed in the tip vortex locations within plane 1, and these values were upwards of 40%. Interestingly, due to the scale of the contours in figures 5.23 and 5.24, the shear layer effect of the rotor base explained in a previous section was not evident in these plots (as the turbulence intensity from the stand base was only approximately 4% in plane 4). In all tests with rotors, regardless of crossflow configuration, a phenomenon was noted in the lower z regions ($0.9 < \frac{z}{R_r} < 1.2$) where there is an area of significantly heightened turbulence intensity. Looking into this phenomenon further, it was determined that this is the result

of ground effect. The bottom of the test domain is located 8.5 inches from the base of the wind tunnel, which causes this ground effect backwash in downstream planes.

Tip Vortex Displacements

One of the primary goals of this project is to determine the displacement of rotor tip vortices in the downstream wake planes, while at the same time, analyzing how the turbulence intensity changes at furthering downstream planes.

To successfully draw these conclusions, the location of each tip vortex in each of the four planes can be plotted as shown in figures 5.26 and 5.27 below. It is important to note that, in this analysis, only the outermost top vortices were analyzed. In the following analysis, 'LT' corresponds to the tip vortex created by the retreating side of the left rotor (rotor 1), and 'RT' corresponds to the tip vortex created by the retreating side of the right rotor (rotor 2) . In this analysis, the two inner tip vortices were not analyzed, as the rotor-rotor interaction caused too much conglomeration of flows, making it too difficult to determine the position of a vortex in any given plane.

The calculation of error, especially in position measurements, is important in this analysis. For a given experimentally-found location measurement, there are two primary sources of error: Velmex Actuator positional error (2 dimensions):

$$\delta E_{1-D} = \pm 0.003"$$

$$\delta E_{2-D} = \pm\sqrt{\delta E_{1-D}^2 + \delta E_{1-D}^2} = \pm 0.0042"$$

Linear interpolation of tip vortex location:

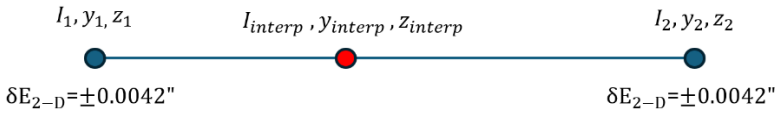

Figure 5.25. Tip vortex lateral or vertical location calculation.

$$I_{interp} - I_1 = \frac{I_2 - I_1}{y_2 - y_1}(y_{interp} - y_1) \quad (16)$$

The error value from the actuator manufacturer was used to determine the 2-D error for the position of the actuator at any given time. These errors feed into figure 5.25 and associated equation 16, which shows the linear interpolation method used to determine the lateral or vertical location of a tip vortex with the given grid coarseness. To extract the approximate position of the tip vortex, the maximum two values of turbulence intensity were taken within each of the two

slipstreams near the leftmost and rightmost rotor tips. From here, equation 16 was used to interpolate these values to the position of the grid. This allows for a positional estimate of the tip vortex core to be estimated with an error that was found to be ± 0.40 inches. For turbulence intensity, a similar method of interpolation was used. Here, instead of a position error feeding into the interpolation error, the turbulence intensity roundoff error ($\pm 0.0005\%$) was used.

The following figures show the results found for lateral and vertical displacements of the vortices for both rotor configurations. Turbulence intensity is also plotted adjacently to determine if crossflow influences the dissipation of turbulence in the downstream.

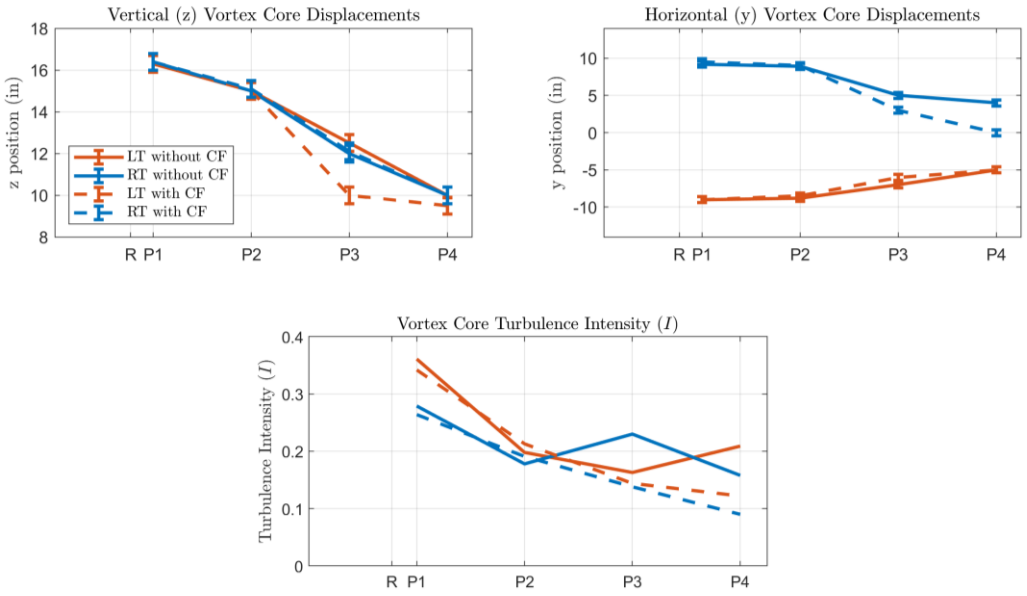

Figure 5.26. COTS configuration tip vortex displacement and turbulence dissipation results.

From figure 5.26, many vortex dynamics relationships can be shown. As stated in the hypothesis of this project, equations 1 and 2 were hypothesized to describe the kinematic relationship between the flow velocity vector and a vortex core position in time. Substituting displacement values found in the results for the COTS rotors in figure 5.26 into equations 1 and 2, the following relationships can be made:

$$\vec{V}_{wind} = [29.1]\hat{\imath} - [15]\hat{\jmath}$$

$$t = 0.0559s$$

$$\Delta y_{core,hypothesis} = -10.06\ in$$

From figure 5.26, the experimental value of right tip vortex displacement and associated error was determined as follows:

$$\Delta y_{core,experimental} = -4.1\ \pm 0.4in$$

As shown in these relationships, it was found the vortex cores from this crossflow experiment moved with an average lateral velocity that was ~60% slower than the hypothesized lateral velocity, and it displaced a total of $\Delta y_{core,experimental}$ more than the case of no crossflow. It was hypothesized that the core would move with exactly a velocity of U_{cross}. With this, it can be inferred that there is an inertial mechanism within a vortex core which makes it so that a vortex core must accelerate from an initial velocity of 0, up to the lateral velocity of U_{cross}. While it can be shown that this is evident from experimentation, the aerodynamic reasoning for this phenomenon is out of the scope of this project.

Referring to the bottom section of figure 5.26, results also showed that there was higher turbulence intensity dissipation rate for the case of crossflow as compared to no crossflow. In the case of no crossflow, turbulence intensity in the rightmost tip vortex decreased by 13.7% from planes 1 to 4 without crossflow, and by 19.7% with crossflow. This confirms the hypothesis that states turbulence decay rate will be increased with crossflow gust impingement on the flow. In the case of the COTS rotors, ΔI_{P1-P4} was found to be -6.0%.

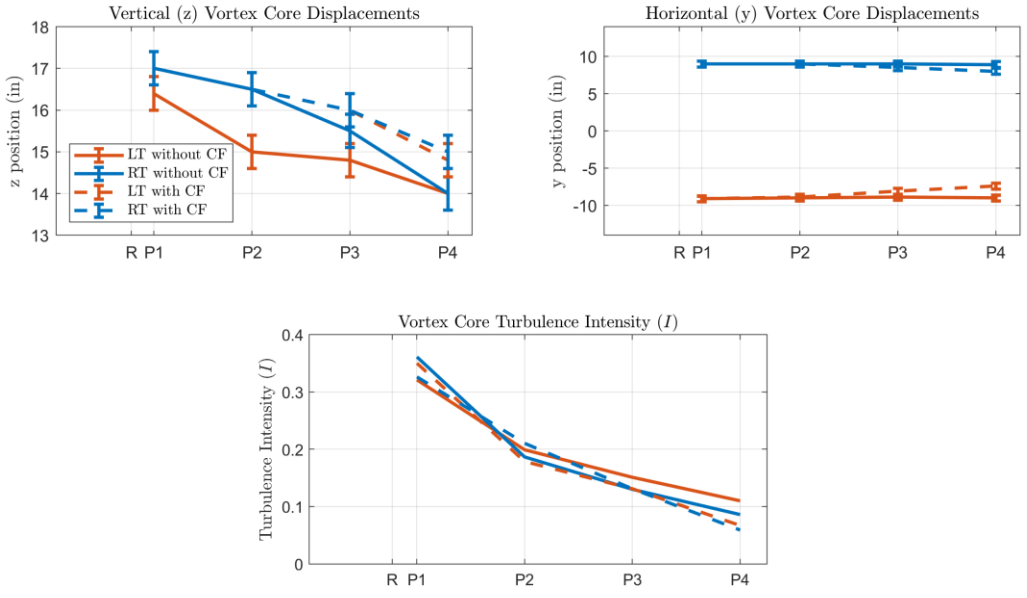

Figure 5.27. NACA configuration tip vortex displacement and turbulence dissipation results.

As shown in figure 5.27, it was found that the rotor wake for the NACA rotors behaved much differently than that of the COTS rotors. Most notably, tip vortices for this configuration behaved 'stiffer' and were more resistant to crossflow gust impingement. As shown, the right tip vortex core displacement difference between without/with crossflow experiments was found to be as follows:

$$\Delta y_{core,experimental} = -0.6\ in \pm 0.4in$$

It was also found that slipstream contraction is almost exactly equal to 0 inches for the experiments without crossflow. The most probable rationale for this is the difference in velocity surpluses shown in figure 5.21 and 5.22. Overall, the NACA rotors produce less than 50% of the thrust generated by the COTS rotors, therefore overall vortex strength is lower in all regions of the wake.

Integral Time Scales

To gain a better understanding of the nature of turbulence for all flight regimes, an integral timescale (τ) analysis was completed on all velocity field data. The integral time scale of a flow field is similarly named 'eddy roll over time', and it can be a good indicator of the time it takes for one eddy to completely roll over in a given dimension [26] From this, estimates of the eddy size can possibly be derived from a combination of turbulence intensity, RMS, and integral time scale. Applying this concept more to the overall goal of this project, this quantification can provide insight into the frequencies of aerodynamic instabilities to be experienced by other vehicles flying within the wake of vehicle in question.

In this analysis, the u and v integral time scales, τ_u and τ_v respectively were calculated using the following analytic methods:

Firstly, the u and v autocorrelation functions, $\rho_u(\tau)$ and $\rho_v(\tau)$, respectively for each grid location 10-second temporal data are calculated using the following equations:

$$\rho_u(\tau) = \frac{\overline{u'(t)u'(t+\tau)}}{\overline{u'(t)u'(t)}} \tag{17}$$

In equation 17, τ represents the integral timescale variable, which is plotted along the x-axis of each autocorrelation function. For simplicity, only the u autocorrelation methods are presented. Breaking down equation 17 further, the numerator and denominator are solved as follows:

Numerator:

$$\overline{u'(t)u'(t+\tau)}(i,1) = \sum_{i=1}^{K}\left(\sum_{j=1}^{N-1}\left(u_j + u_{j+1}\right)\right) \tag{18}$$

Where i and j are the timescale and velocity indices, respectively.

Denominator:

$$\overline{u'(t)u'(t)} = \frac{1}{N_{Data}}\sum_{i=1}^{k} u_k^2 - \left(\frac{1}{N_{Data}}\sum_{i=1}^{k} u_k\right)^2 = \rho_u(1) \tag{19}$$

The denominator of equation 17 is the initial (t = 0) value of the autocorrelation function, which serves as means of nondimensionalization of the overall autocorrelation function. After the autocorrelation function has been calculated for a given temporal velocity dataset, the integral timescale can be calculated by integrating the autocorrelation function up until the decorrelation point, which is where the autocorrelation function first crosses the τ axis. A trapezoidal integration method was implemented through Matlab using the following equations:

$$\tau_{I,u} = \int_0^{\tau,\rho=0} \rho_u d\tau \tag{20}$$

After running these calculations for each of the flight configurations, the integral timescale results can be plotted on a contour, and these results are shown in figures 5.28 and 5.29 for the COTS and NACA configurations below:

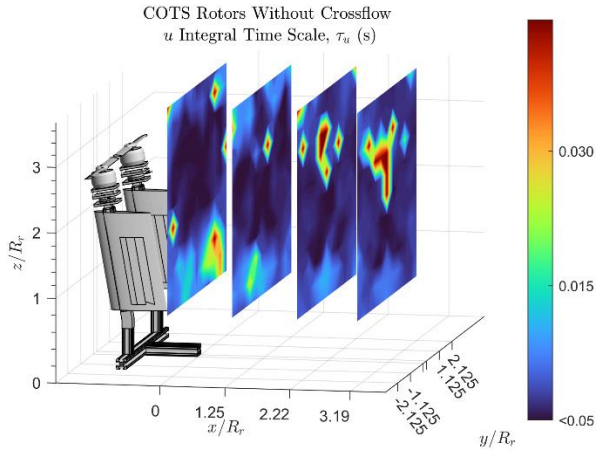

(a.)

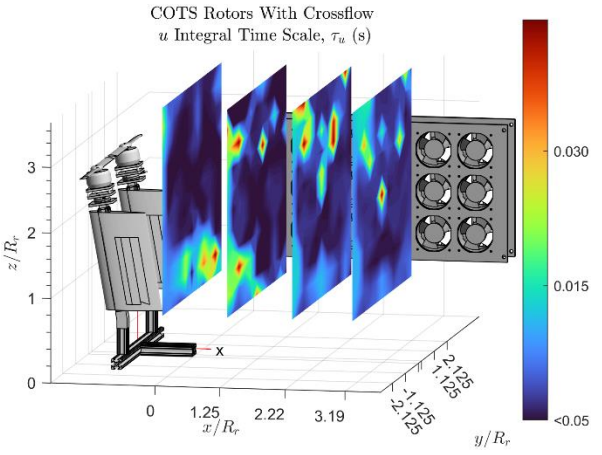

(b.)

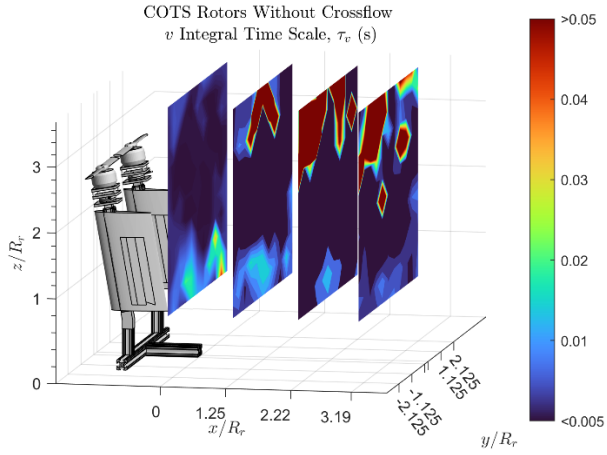

(c.)

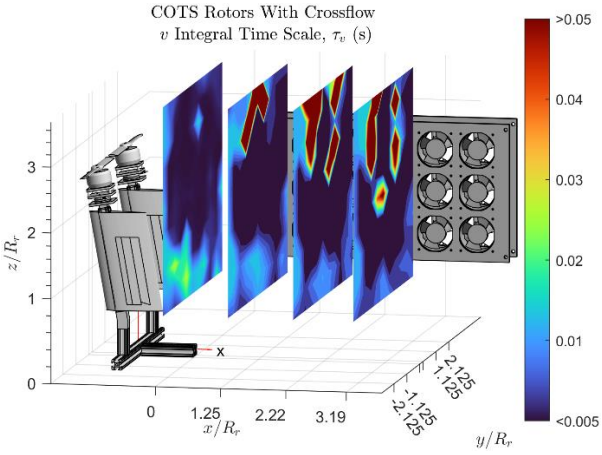

(d.)

Figure 5.28. COTS configuration u and v integral timescale results (a.) τ_u COTS w/o crossflow (b.) τ_u COTS with crossflow (c.) τ_v COTS w/o crossflow (d.) τ_v COTS with crossflow.

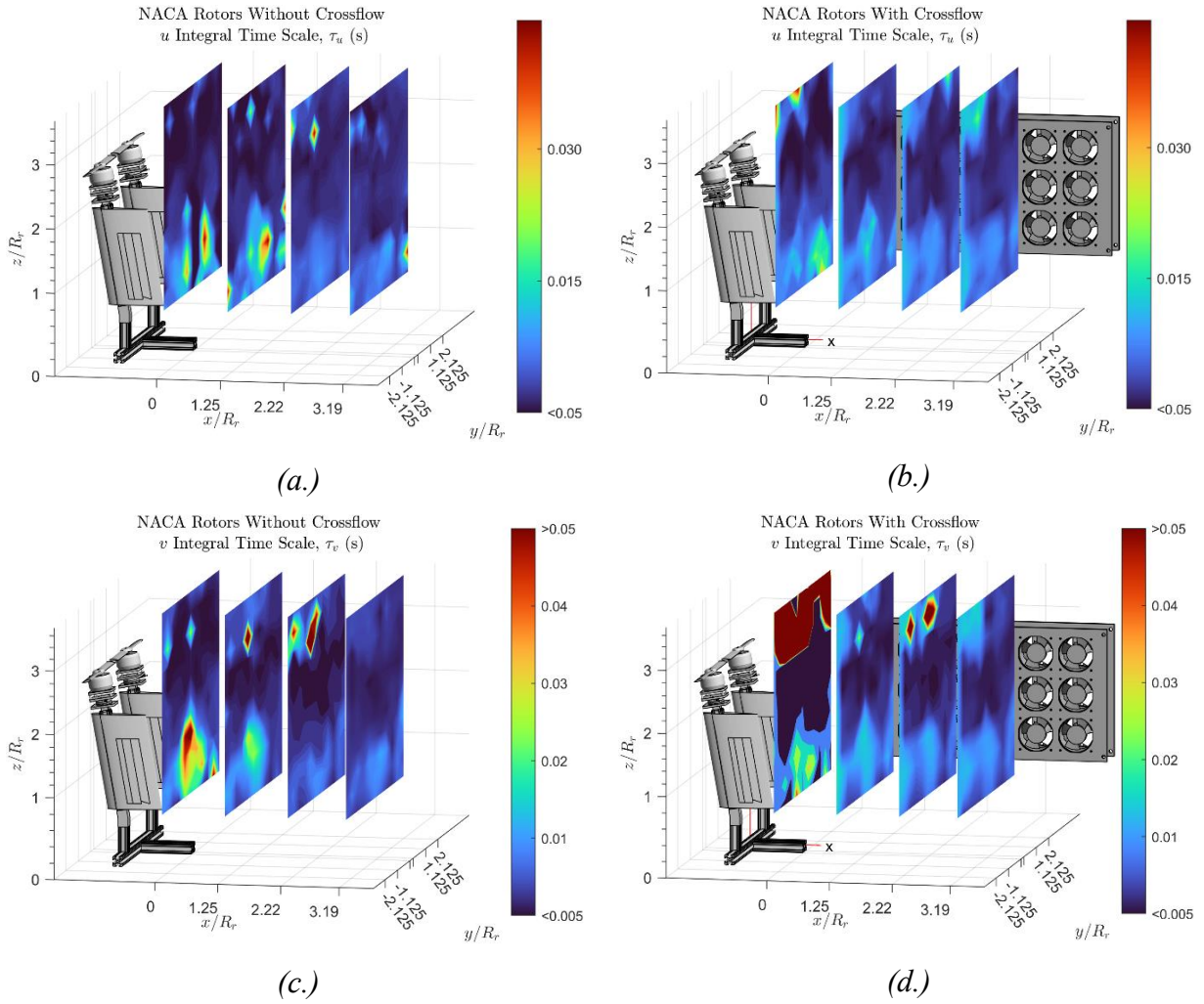

Figure 5.29. NACA configuration u and v integral timescale results (a.) τ_u NACA w/o crossflow (b.) τ_u NACA with crossflow (c.) τ_v NACA w/o crossflow (d.) τ_v NACA with crossflow.

As made evident in figures 5.28 and 5.29, the u(longitudinal) timescales are nearly a full order higher than that of the v (lateral) timescales. This shows that any given eddy in the x direction will roll over 10 times faster than the same eddy in the y direction. This aligns with the flow regime theory that has been built in this experiment. The majority of the flow is being moved in the x direction, while vortex-shed eddies contribute a huge amount of mass flow in the y and z axes, which is shown in the velocity contours presented earlier.

Figures 5.28 and 5.29 above show that within the rotor wakes, especially near tip vortices, τ_u and τ_v both decrease drastically. This is an intriguing finding that shows that eddies and more specifically, tip vortices within this region of the flow are rolling over much quicker than outside of the wake of the rotors.

While the effect of crossflow gust on integral timescale was found to be very small, there is still a minute difference in the in the no crossflow vs. crossflow case, which is evident in figure 5.28 and 5.29 b.) and d.) for both rotor configurations. Overall, it was found that for both rotor configurations, crossflow gust increased the integral timescale of the flow, especially in planes 3 and 4 which are further downstream. Comparing these results to the turbulence intensity results, it can be concluded that the turbulence intensity and integral timescale are inversely related, as turbulence intensity decreases with furthering downstream planes (especially for the case of crossflow gust), while integral timescale increases with furthering downstream planes.

Loads Testing

As shown in figure 5.1, loads testing results determined the thrust coefficients for both sets of rotors, both in hover and forward flight. The testing was conducted by taking a time average of the vertical force (in the direction of tilt of rotors) produced by the rotors. The primary results of these tests showed that the COTS rotors produced more than two times the thrust of the COTS rotors. As discussed above, correlations could be made between the thrust generated and the strength/magnitude of wake turbulence in the planes analyzed.

CHAPTER 6. Conclusions

Summary of Results

Ambient wind tunnel tests without rotors showed that the flow is overall primarily unform across the testing domain. As discussed, there was a region of recirculating flow emanating from the shear layer that broke off from the rotor rig base. It was found that the effects of this phenomenon were minimal on the wake of the rotors.

For the case of wind tunnel ambient with crossflow, overall, it was found that the crossflow generator energizes the flow and contributes to increased turbulence intensity (~3% higher), especially in the downstream planes. As expected, it was also found that the crossflow generator provides velocity surpluses in the negative y direction, especially on the right side of the testing domain closest to the crossflow fans.

Velocity contour results for tests with rotors showed that there are drastically high velocity surpluses in regions of the flow where wake vortices are prominent for all rotor planforms. These findings carried over and were also shown in the turbulence intensity plots. Not only were the velocity surpluses in these regions high, but the overall turbulence in these regions was heightened.

Comparing rotor planforms, it was found that the COTS rotors had drastically higher velocity surpluses throughout the entirety of the wake than the NACA rotors. This was an intriguing and unexpected finding. With crossflow, the overall turbulence intensity of the right side of the wake (near the crossflow fans) experienced a generally lower intensity than in the case of without crossflow for both rotor planforms. Furthermore, for both rotor planform cases, it was found that there is a lateral displacement difference between the cases of with and without crossflow. Vertically, the slipstream geometry stays similar and close to expected location values from literature both with and without crossflow.

Overarching Conclusions

Overall, the effects of crossflow impingement were well characterized within this project. Firstly, the hypothesis set forth of tip vortices propagating laterally precisely with the velocity of the crossflow generator was disproved. In the cases of both rotor planforms, the tip vortices propagated laterally much less than hypothesized. Instead of the simple, zero acceleration kinematic relationship shown in equation 2, a term must be added to properly describe the position of a given vortex under the influence of crossflow gust, as shown in equation 21, below.

$$\Delta y_{core} = [\vec{V}_{core}]\hat{j} \cdot t + \frac{1}{2}[\vec{a}_{core}(t)]\hat{j} \cdot t^2 \quad (21)$$

The second term in this equation shows the different term that must be added to solve this relationship. While this term is present, $[\vec{V}_{core}]\hat{j}$ cannot be set simply as the crossflow velocity set in the experiments, which is $U_{cross} = 15\frac{ft}{s}$. More specifically, the $[\vec{V}_{core}]\hat{j}$ term must be represented as a function of plane number. For example, lateral velocity at plane 1 should be extracted directly from figure 5.15 (a.), as well as the respective velocities from the other planes. From here, $[\vec{V}_{core}]\hat{j}$ can be compiled into a piecewise function that contains values at each plane, at which point the displacements of tip vortices can be added to each other.

Relating to the results presented on turbulence intensity in the wake, it was found that there are drastically higher regions of turbulence intensity within tip vortices and vortex sheet regions for both rotor planforms. Turbulence intensity was found to decay much faster and more effectively in the tests with crossflow impingement, which confirms the hypothesis relating to turbulence dissipation.

Future Work

There is substantial room for future work and expansions to this project and Thesis. Relating to the experimental results, there must be more work completed on the competency of the crossflow gust generation and impingement on the wind tunnel flow. A test determining the effectiveness of the generator at different gust speeds is necessary to fully assess the crossflow speed on the other side of the testing domain. While the crossflow gust generator acted on the flow on the right side of the wind tunnel vigorously, the crossflow generator was found to act more as a 'boundary layer energizer' than a constant crossflow generator. Examining how increasing the speed of the crossflow gust affects the freestream flow is a future project that could give more closure to the exact velocity profile of the wind tunnel flow and better validate the results of this project.

As for future related work, the most ambitious but practical project could be an extension of this project focused on the aerodynamic interactions of skyscrapers or large buildings on EVTOL aircraft. While the aerodynamics of large buildings are well understood, it is difficult to predict the unsteadiness of skyscraper wakes in the presence of high winds. Work has been completed on this topic in the past [27], but expanding on this area of research in the sense of UAM and rotor aerodynamics is an area of great interest.

REFERENCES

[1] Pearson, M., “How far are people on average from their nearest decent-sized airport?” 2012. https://doi.org/AverageDistancetoNearestAirport(mark-pearson.com).

[2] McAuliffe, B., Barber, H., and Ghorbanishohrat, F., “The influence of traffic wakes on the aerodynamic performance of heavy duty vehicles,” SAE Int. J. Advances Curr. Prac. In Mobility, 2023, pp. 2208–2211. https://doi.org/10.4271/2023-01-0919.

[3] Nguyen, N., Bartolini, G., Baculi, G., Okolo, W., and Xiong, J., “Wake Vortex Interaction of Urban Air Mobility Aircraft,” AIAA Acitech 2022 Forum, Vol. 22, No. 2376, 2021, pp. 3–26. https://doi.org/10.2514.

[4] “NTSB Aviation Accident Final Report,” Accident Number WPR22LA072,, 2022, pp. 1–5. https://doi.org/NTSBDocket-DocketManagementSystem.

[5] “Safety Risks From Rotor Wash at Hospital Helicopter Landing Sites,” 2023, pp. 1–13. https://doi.org/NTSBDocket-DocketManagementSystem.

[6] Board, N. T. S., “AA587 Aircraft Accident Report,” PB2004-910404, 2004, pp. 133–162. https://doi.org/NTSBDocket.

[7] By Evans, H., and Lowell, “AA587 Flight Path Information,” CC BY-SA 4.0 from Wikipedia, 2004, https://commons.wikimedia.org/w/index.php?curid=147302982.

[8] Leishman, J., Principles of Helicopter Aerodynamics, 2nd ed., Cambridge University Press, United Kingdom, 2006, Chaps. 7, 3, p. 350.

[9] Landgrebe, A., “The Wake Geometry of a Hovering Helicopter Rotor and Its Influence on Rotor Performance,” J. Am. HelicopterSoc, Vol. 17, 1972, pp. 3–15. https://doi.org/10.4050/JAHS.17.4.3.

[10] Tulwin, T., “Low Reynolds Number Rotor Blade Aerodynamic Analysis,” MATEC Web of Conferences, Vol. 252, No. 04006, 2019, pp. 1–3. https://doi.org/10.1051.

[11] Trainor, G., “Helicopter Wake Turbulence,” Cleared for Takeoff, 2023.

[12] Hoydonck, W., Haverdings, H., and Pavel, M., “A Review of Rotorcraft Wake Modeling Methods for Flight Dynamics Applications,” 35th European Rotorcraft Forum Proceesings, 2009, pp. 32–40. https://doi.org/101221.

[13] Stone, C., E, D., and Gharakhani, A., “Towards a coupled Eulerian/Lagrangian simulation method for rotorcraft wake modeling,” Aerospace Sciences Meeting and Exhibit, Vol. 2008, No. 659, 2008, p. 7. https://doi.org/10.2514/6.2008-659.

[14] Lee, H., “Review of vortex methods for rotor aerodynamics and wake dynamics,” Advances in Aerodynamics, Vol. 4, No. 1, 2022, pp. 8–29. https://doi.org/10.1186/s42774-022 00111-3.

[15] Martin, P., Pugliese, G., and Leishman, J., “High Resolution Trailing Vortex Measurements in the Wake of a Hovering Rotor,” Journal of the American Helicopter Society, Vol. 48, No. 1, 2023, pp. 39–52. https://doi.org/10.4050/JAHS.48.39.

[16] Yao, T., Zhou, S., and Ye, S., “Design and Test of an Integrated Measurement System for Multi-Hole Probe Calibration and Vortex Measurement,” Sensors Journal, Vol. 22, No. 2376, 2022, pp. 8–11. https://doi.org/10.3390/s22062376.

[17] Miller, N., and Beresh, S., “Using Particle Image Velocimetry to Determine Turbulence Model Parameters,” AIAA Journal, Vol. 59, No. 3, 2021, pp. 843–851. https://doi.org/10.2514/1.J059741.

[18] Ansaripour, M., Dafsari, R., Yu, S., Choi, Y., and Lee, J., “Characteristics of a tip-vortex generated by a single rotor used in agricultural spraying drone,” Experimental Thermal and Fluid Science, Vol. 149, No. 110995, 2023, pp. 3–8. https://doi.org/10.1016.

[19] Lee, S., Chae, S., Woo, S., Jang, J., and Kim, J., “Effects of Rotor-Rotor Interaction on the Wake Structure and Thrust Generation of a Quadrotor Unmanned Aerial Vehicle,” IEEE Access, Vol. 9, 2021, pp. 85995–86016. https://doi.org/10.1109/ACCESS.2021.3088150.

[20] Theys, B., Dimitriadis, G., Hendrick, P., and De Schutter, J., “Experimental and Numerical Study of Micro-Aerial-Vehicle Propeller Performance in Oblique Flow,” Journal of Aircraft, Vol. 54, No. 3, 2017, pp. 1076–1080. https://doi.org/10.2514/1.C033618.

[21] Erhard, R., and Alonso, E., “Comparison of Propeller Wake Models for Distributed Electric Propulsion and eVTOL Aircraft in Complex Flow Conditions,” AIAA Journal, 2022, pp. 6–11. https://doi.org/10.2514/6.2022-1676.2

[22] Hwang, J., Jung, M., and Kwon, O., “Numerical Study of Aerodynamic Performance of a Multirotor Unmanned-Aerial-Vehicle Configuration,” Journal of Aircraft, Vol. 52, No. 3, 2015, pp. 842–845. https://doi.org/10.2514/1.C032828.

[23] Shastry, A., and Datta, A., “Predicting Wake and Structural Loads in RPM Controlled Multirotor Aircraft,” Vertical Flight Society, 2020, pp. 1–12.

[24] Caprace, D., Ning, A., Chatelain, A., and Winckelmans, G., “Effects of rotor-airframe interaction on the aeromechanics and wake of a quadcopter in forward flight,” Aerospace

Science and Technology, Vol. 130, No. 107899, 2022, pp. 6–15. https://doi.org/10.1016/j.ast.2022.107899.

[25] Inomata, C., and Kuwata, M. e. a., “Model position sensing method for low fineness ratio models in a magnetic suspension and balance system,” Nature Communications, Nat Commun, pp. 1–6. https://doi.org/10.1038/s41467-023-42213-6.

[26] Pope, S. B., Turbulent Flows, 1st ed., Cambridge University Press, United Kingdom, 2000, Chap. 3, pp. 30–100

[27] Fukami, K., and Taira, K., “Grasping extreme aerodynamics on a low-dimensional manifold,” Nature Communications, Nat Commun, pp. 1–6. https://doi.org/10.1038/s41467-023-42213-6.

Appendix A. Parse_Data.m

```
 %% Program Explanation

% The following code takes a 7-hole probe raw data file and breaks out the
% 11x11 time based grid locations from a large data set. The output is a
% cell array with each top entry corresponding to the following locations:

% each point contains 10 seconds worth of 7-hole data time history

% {main output} = (y, z) points correspond to location in cell array

function [cellar_pressure_data] = Parse_Data(traverse_filename)

addpath('Raw Data Files');
addpath('Processors');
addpath('PostProcess_7-Hole_Data');
cellar_pressure_data = cell(11, 11);
data = readmatrix(traverse_filename);

%time = data(:, 1);  % full time history (~3112.26 seconds)
time_count_0 = 0; % lower timestep
time_count_f = 12; % upper timestep

% Timming constants
dty = 7.27; % time to move 3 inches in y
% dtz = 5.03; % time to move 2 inches in z
dtz = 6.03; % time to move 2 inches in z with an extra 1s offset
dtdata = 12; % time for each data aquisition
dtlong = 73.07; % time to reset to ymin from ymax

% Parse Data into cell array
for z = 1:11
    for y = 1:11
        bool = data(:, 1) >= (time_count_0 + 1) &... % 1 second cushion
               data(:, 1) <= (time_count_f - 1);     % 1 second cushion
        cellar_pressure_data{y, z} = data(bool, :);  % Parse
        if y == 11 % don't increment dty on final move
            time_count_0 = time_count_0 + (dtdata); % increment time
            time_count_f = time_count_f + (dtdata); % incrememement time
        else
            time_count_0 = time_count_0 + (dtdata + dty); % increment time
            time_count_f = time_count_f + (dtdata + dty); % incrememement time
        end
    end
    time_count_0 = time_count_0 + dtlong; % time to get back to ymin
    time_count_f = time_count_f + dtlong; % time to get back to ymin
    time_count_0 = time_count_0 + dtz; % time to raise 2 in in z
    time_count_f = time_count_f + dtz; % time to get 2 in in z

end
end
```

Appendix B. Seven_Hole_Processing_Joseph.m

```
%% Program Explanation

% The following code takes an 11x11 cell array of transient 7-hole data
% and processes the data using nhole()
% Inputs:
%   traverse data, 11x11 grid with proper time spacings
%   7-Hole model specific calibration file (.xlsx)
% Outputs:
%   11x11 cell array
%       each (y, z) location has 4 columns: time (s), U, V, W (ft/s)

function [cellar_velocity_data] =...
    Seven_Hole_Processing_Joseph(traverse_filename, calibration_filename)
    %% Pathing
    addpath('PostProcess_7-Hole_Data');
    addpath('Raw Data Files');
    addpath('Processors');

    %% Independent Variables and Constants
    R = 8.31446;
    Mv = 0.018016;
    Md = 0.0289652;
    cellar_velocity_data = cell(11, 11); % pre-allocate
    %% Read in Data
    cellar_pressure_data = Parse_Data(traverse_filename);
    calib_file = readmatrix(calibration_filename);
    gencalpsi = calib_file(:,1); % use the specific calibration file for our probe
    gencalthe = calib_file(:,2); % it's called "SN1051.xlsx"
    calpres = calib_file(:,3:9);
    calvinf = calib_file(:,10);
    calrho = calib_file(:,11);
    calPatmos = calib_file(:, 12);

    parfor z = 1:11
        for y = 1:11
            time = cellar_pressure_data{y, z}(:, 1);
            P0 = cellar_pressure_data{y, z}(:, 2);
            P1 = cellar_pressure_data{y, z}(:, 3);
            P2 = cellar_pressure_data{y, z}(:, 4);
            P3 = cellar_pressure_data{y, z}(:, 5);
            P4 = cellar_pressure_data{y, z}(:, 6);
            P5 = cellar_pressure_data{y, z}(:, 7);
            P6 = cellar_pressure_data{y, z}(:, 8);
            P_data = [P0, P1, P2, P3, P4, P5, P6]; % Measured pressure array
            T_thermistor = cellar_pressure_data{y, z}(:, 9);
            P_amb = cellar_pressure_data{y, z}(:, 10);
            T_sensor = cellar_pressure_data{y, z}(:, 11);
            humdata = cellar_pressure_data{y, z}(:, 12);
            Nx = cellar_pressure_data{y, z}(:, 13);
            Ny = cellar_pressure_data{y, z}(:, 14);
            Nz = cellar_pressure_data{y, z}(:, 15);
            wx = cellar_pressure_data{y, z}(:, 16);
```

```
            wy = cellar_pressure_data{y, z}(:, 17);
            wz = cellar_pressure_data{y, z}(:, 18);

            % Data reduction
            accdata = cellar_pressure_data{y, z}(:,13:15);

            phidata = atan2(accdata(:,2),sqrt((accdata(:,1).^2) +...
                          (accdata(:,3).^2)));
            thethdata = atan2(accdata(:,1),sqrt((accdata(:,2).^2) +...
                            (accdata(:,3).^2)));

            phiavg = mean(phidata);
            thethavg = mean(thethdata);

            % Calibration and Velocity Components
            calthe = (gencalthe.*cos(phiavg)) - (gencalpsi.*sin(phiavg));
            calpsi = (gencalthe.*sin(phiavg)) + (gencalpsi.*cos(phiavg));
            fincal = [calpsi, calthe, calib_file(:,3:end)];

            caltotpres = ones(size(calpsi)).*((1/2).*calrho.*(calvinf.^2));
            calstatpres = zeros(size(calpsi));

            % Naming variables for calculations below
            dataarray = [cellar_pressure_data{y, z}(:,1:8),...
                         (cellar_pressure_data{y, z}(:,9) + 273.15),...
                         cellar_pressure_data{y, z}(:,10),...
                         (cellar_pressure_data{y, z}(:,11) + 273.15),...
                         (cellar_pressure_data{y, z}(:,12)./100),...
                         (cellar_pressure_data{y, z}(:,13:15).*9.80665),...
                         cellar_pressure_data{y, z}(:,16:end)];
            dataarraysize = size(dataarray);
            totpresdata = zeros([dataarraysize(1),7]);
            statpresdata = zeros([dataarraysize(1),7]);

            presdata = [dataarray(:,2:8), dataarray(:,10)];
            tempdata = [dataarray(:,9), dataarray(:,11)]; % Temp array
            psat = 6.1078.*(10.^((7.5.*(tempdata(:,1)-273.15))./tempdata(:,1)));
            pv = humdata.*psat;
            pd = presdata(:,8) - pv;
            rhodata = ((pd.*Md)+(pv.*Mv))./(R.*tempdata(:,1));
            %% Process Data
            ngrid = 200;

            [U, V, W, ~] = nholeGT(calthe, calpsi, calpres, caltotpres,
calstatpres,...
                P_data, 0, 0, rhodata, ngrid); % m/s output
            cellar_velocity_data{y, z}(:, 1) = time;
            cellar_velocity_data{y, z}(:, 2) = U*3.28084; %ft/s
            cellar_velocity_data{y, z}(:, 3) = V*3.28084; %ft/s
            cellar_velocity_data{y, z}(:, 4) = W*3.28084; %ft/s


        end
    end
end
```